

Altered patterning of neural activity in a tauopathy mouse model

C. Hoffman¹, J. Cheng², R. Morales¹, D. Ji², Y. Dabaghian¹

¹*Department of Neurology,
The University of Texas McGovern Medical School,
6431 Fannin St, Houston, TX 77030*

²*Department of Neuroscience,
Baylor College of Medicine, Houston, TX 77030,*

**e-mail: Yuri.A.Dabaghian@uth.tmc.edu*

(Dated: March 26, 2024)

Alzheimer's disease (AD) is a complex neurodegenerative condition that manifests at multiple levels and involves a spectrum of abnormalities ranging from the cellular to cognitive. Here, we investigate the impact of AD-related tau-pathology on hippocampal circuits in mice engaged in spatial navigation, and study changes of neuronal firing and dynamics of extracellular fields. While most studies are based on analyzing instantaneous or time-averaged characteristics of neuronal activity, we focus on intermediate timescales—spike trains and waveforms of oscillatory potentials, which we consider as single entities. We find that, in healthy mice, spike arrangements and wave patterns (series of crests or troughs) are coupled to the animal's location, speed, and acceleration. In contrast, in tau-mice, neural activity is structurally disarrayed: brainwave cadence is detached from locomotion, spatial selectivity is lost, the spike flow is scrambled. Importantly, these alterations start early and accumulate with age, which exposes progressive disinvolvement the hippocampus circuit in spatial navigation. These features highlight qualitatively different neurodynamics than the ones provided by conventional analyses, and are more salient, thus revealing a new level of the hippocampal circuit disruptions.

Significance. We expose differences in WT and tau brains, emerging at the circuit level, using a novel, morphological perspective on neural activity. This approach allows identifying qualitative changes in spiking patterns and in extracellular field oscillations, that are not discernible through traditional time-localized or time-averaged analyses. In particular, analyses of activity patterns facilitates detection of neurodegenerative deviations, conspicuously linking their effects to behavior and locomotion, thus opening a new venue for understanding how the architecture of neural activity shifts from normal to pathological.

I. INTRODUCTION

Alzheimer’s Disease (AD) is a devastating neurodegenerative condition that is extensively studied at multiple levels, from molecular, to cellular, to organismal [1–3]. It is particularly challenging to understand how all these levels connect and to identify which functional intermediaries link neural pathologies to cognitive deterioration. For instance, it is believed that $A\beta$ -plaques and neurofibrillary tangles disrupt the synergistic coordination of circuit dynamics [4, 5]. However, their subsequent contribution to the observed behavioral symptoms of AD remain unclear [6–9]. Many studies of AD-related changes of spiking activity and synchronized extracellular field dynamics reveal disturbances, including alteration of neuronal firing rates [10, 11], slowing of brainwave rhythms [12, 13], reductions in signal complicacy [14], and increased epileptiform activity [15–20]. Despite these efforts, systemic insight into the circuit-level impact of AD pathologies is still lacking due to the prohibitive complexity of the network dynamics, sheer amount of interconnected elements, and intricacy of interactions which render detailed data analyses and realistic modeling nearly intractable.

On the other hand, this very intricateness begets simplification by bringing forth statistical aspects of circuit activity. As it turns out, large pools of spike trains and waveforms exhibit universal statistical properties that have generic, mathematical origins, independent from the underlying physiological mechanisms. The ways in which these statistics unfold in time open a new venue for examining circuit dynamics differences between normal and pathological brains.

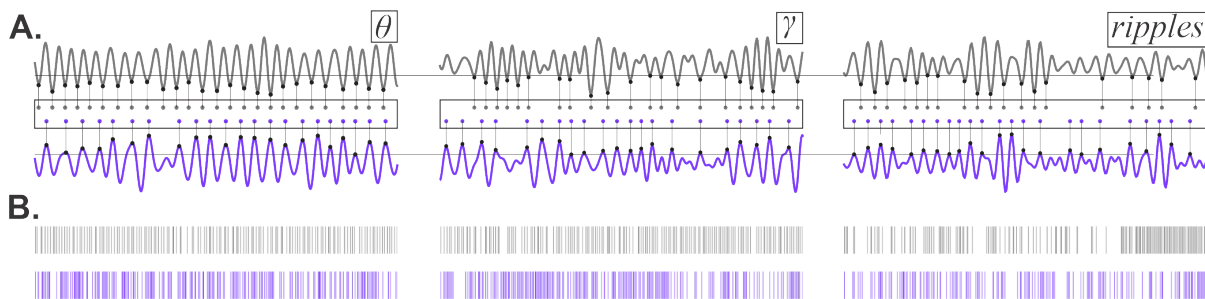


FIG. 1. Patterns of neural activity in wild type (WT) and mice affected by brain tauopathy. **A.** LFP waves recorded in WT (gray trace) and tau (purple trace) mice, with their significant peaks and troughs marked by dots, boxed. Differences between the resulting patterns are apparent, although the waves are scaled to the same frequencies and amplitudes. The shapes of the waves are easily recognizable, *e.g.*, the ones on the left, marked “ θ ,” correspond to the θ -waves (4 – 12 Hz). Would it be surprising if they were marked as “ γ ” (30 – 80 Hz) or “ripples” (150 – 250 Hz)? How surprising? Also note that tauopathic θ -waveforms are somewhat less regular than the WT θ -waveforms, whereas WT’s γ - and ripple waveforms appear more cluttered than in tau-mice. Could these differences be attributed to random fluctuations of the waves’ shapes or should they be taken as signatures of qualitative changes? How to capture the morphological differences mathematically? **B.** Spike trains recorded from WT (gray) and tau (purple) interneurons also demonstrate different patterns, suggesting that tau-pathologies alter the flow of information exchange.

In this study, we consider neuronal spike trains and waveforms of locally recorded extracellular field potentials (LFP) as basic observables characterizing circuit dynamics. We analyze these temporally extended entities without averaging, evaluating their instantaneous behavior, or decomposing into simpler constituents. Instead, we use certain morphological properties of data segments to obtain their integral descriptions at structural level, which opens a new narrative and creates new perspectives on the underlying physiological phenomena. As an illustration of our approach, consider the brainwaves illustrated on Fig. 1A, which are scaled to same mean amplitude

and frequency range. Yet, they are visibly different: one could argue, *e.g.*, that top waves are more regular, with stereotypical undulatory shapes, or perhaps more ordered. Similarly, the spike trains shown on the top of Fig. 1B are less cluttered, less haphazard and more uniform than their bottom counterparts. Surprisingly, these intuitive distinctions can be captured formally and used for quantifying neurodynamics [21]. In the following, we apply these methods to study hippocampal activity in a mouse model of tau pathology and extracted a number of constitutive, pathological deviations of their circuit activity.

II. METHODS

Experimental procedures. Spike and LFP data were recorded from the hippocampal CA1 area of healthy wild type (WT) and transgenic mouse models of tau pathology (rTg4510). rTg4510 mice which develop tau neurofibrillary tangles and neuronal loss similar to those observed in human tauopathies [22, 23]. The animals were trained in a familiar room to run back and forth on about 2 m long rectangular track for food reward. The daily recording procedure consisted of two 15-minute-long running sessions, followed by 15-minute sleep breaks. The LFP data was sampled at 2 kHz rate and the animals’ positions were sampled at 33 Hz with a resolution of approximately ± 0.2 cm, by tracking two head-mounted color diodes. Further details on the surgery, tetrode recordings and other procedures can be found in [24, 25].

Computational procedures are based on applying two complementary measures.

λ -score, introduced by A. Kolmogorov, quantifies the “randomness” or “haphazardness” of patterns through their deviation from an expected mean trend (Fig. 2A). Remarkably, these deviations exhibit regular statistical behaviors, described by a universal probability distribution, $P(\lambda)$ (Fig. 2B, [26–29]). According to its structure, most patterns produce λ -scores confined between certain limits, *e.g.*, about 99.7% of patterns have λ -scores between $\lambda^- = 0.4$ and $\lambda^+ = 1.8$, and only 0.3% fall outside of these bounds. Thus, the patterns with λ -scores within that range can be qualified as “stochastically typical,” whereas those that fall outside of it are “atypical.”

In practice, the mean trend of recurring neurophysiological activity is often easy to estimate, *e.g.*, one can evaluate the mean rate of LFP oscillations by averaging the number of crests or troughs over sufficiently long periods—such as a running session. However, these trends are known to change with the animal’s physiological state. For instance, the LFP’s overall cadence alters between active movement and quiescence [30–32] (Fig. S1). Correspondingly, the “reference point” for computing the patterns’ statistics also changes. Taking these alterations into account allows for *contextual* λ -scores that produce more nuanced descriptions of circuit dynamics, discussed below.

β -score provides an alternative measure of stochasticity that emphasizes patterns’ orderliness (Fig. 2C). As shown in [27–29], nearly periodic, ordered patterns of n elements produce smaller β -values (the minimal value, $\beta = 1$, is produced by a strictly regular, periodic pattern). Clustering patterns yield larger β -values: the maximum, $\beta = n$, is reached when all elements lump together. As it turns out, impartially scattered patterns produce β -scores close to 2—as a matter of another surprising universality [21, 27].

Curiously, the shapes of the β -distributions, $P_n(\beta)$, albeit n -dependent, are similar to the shape of Kolmogorov distribution, $P(\lambda)$, in one important aspect: they all have a dominant “hump” and rapidly decaying tails (Fig. 2D). Moreover, all β -distributions have similar modes and means, that converge to $\beta^* \approx 2$ as the sample size increases (Fig. M1). One can therefore specify limits, β_n^- and β_n^+ , that confine the “typical” β -scores and exclude the “atypical” ones. For instance, $\beta_{30}^- \approx 1.4$ and $\beta_{30}^+ \approx 3.6$, confines 99.7% of patterns containing $n = 30$ elements (Fig. 2D).

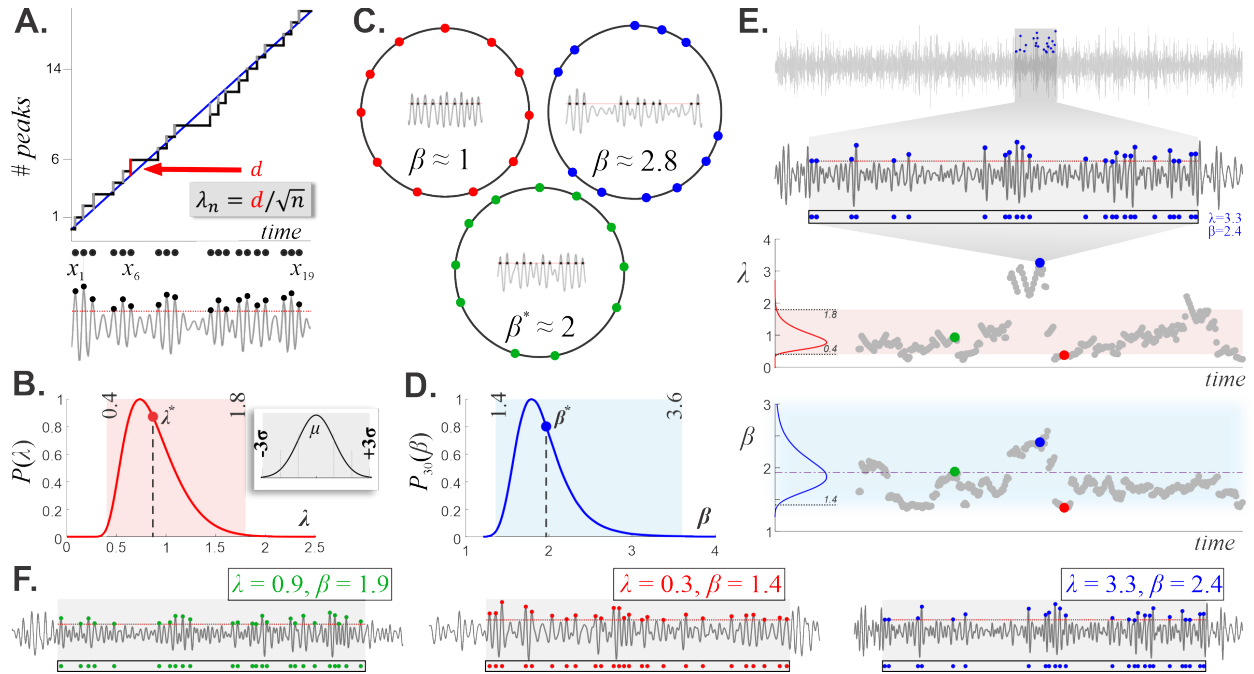


FIG. 2. Pattern statistics. **A.** Given a series of values, $X = \{x_1, x_2, \dots, x_n\}$, *e.g.*, a series of $n = 19$ wave crests shown at the bottom, we build its *empirical distribution*—a staircase that makes a unit step up at each consecutive x_i . The slope of the staircase is defined by the mean trend (blue line), *e.g.* about eight θ -peaks are expected every second. The λ -score of X is the greatest deviation of its points from this trend, normalized by the sample size. **B.** The distribution of λ -scores, $P(\lambda)$, is universal and defines the impartial probability of a given pattern’s appearance. On average, λ -scores are close to $\lambda^* \approx 0.87$; patterns that closely follow the prescribed behavior produce small λ s, and those that deviate significantly from the mean trend have large λ -scores. About 99.7% of patterns score between $\lambda^- = 0.4$ and $\lambda^+ = 1.8$ (pink stripe) and are hence “typical”, whereas patterns with small ($\lambda < 0.4$) or large ($\lambda > 1.8$) λ -scores are “atypical”. The selection of bounds is motivated by analogy with the Gaussian distribution (top panel), in which typical values are those that fall closer than 3σ from the mean (gray stripe, 99.7% of cases) and the atypical ones lay farther out (0.3%). **C.** Placing n elements of X around a circle, summing the squared arc lengths, and normalizing the result by the circumference yields $\beta(X)$. For periodic arrangements (red points) β is small, $\beta \approx 1$, for “clustered” patterns (blue points) β is large (up to $\beta \approx n$), and for generic layouts (green points) $\beta \approx 2$ —a surprising statistical universality. **D.** The distribution of β -values for a pattern, X , of length $n = 30$: similar to λ -scores, typical β values fall between specific bounds $\beta_{n=30}^- = 1.4$ and $\beta_{n=30}^+ = 3.6$. The general form of β -distributions depends on the pattern’s size, as illustrated on Fig. M1D. **E.** Shown are λ (top) and β (bottom) dynamics, evaluated by “sliding” a 25-peak window along a γ -wave. The pink stripe represents the typical range of λ s as on panel B (laid horizontally), and the blue stripe is the same as on panel D. **F.** An example of a “statistically mundane” pattern (green point on panel E, $\lambda = 0.9$ and $\beta = 1.9$) and patterns with small or large values of λ and β (red and blue points on E, respectively).

Dynamics of stochasticity can be computed by evaluating the λ - and β -scores for local data segments, *e.g.*, for waveforms or spike trains contained in a time window of width L , centered at time t . As the window shifts forward in time, this “snapshot” of the data evolves, yielding time-dependent haphazardness, $\lambda(t)$, and orderliness, $\beta(t)$, that describe pattern changes. We emphasize here that circuit dynamics can drive the brain waves into assuming highly improbable waveforms, characterized by very low probabilities of accidental appearance. For example, periodic patterns are too orderly to happen by chance, but they can be enforced by limit cycles in the network’s phase space. In the following, we detect qualitative changes in the hippocampal dynamics by

identifying atypical network patterns.

In order to construct $\lambda(t)$ and $\beta(t)$ dynamics empirically, one can either use a time window of fixed width, shifting it by a pre-specified time step, or adapt the width at each step, so that each window contains a pre-specified number of spikes or LFP peaks (Fig. S2). Numerically, these algorithms differ only marginally, but they catch different aspects of the patterns' statistics. Intuitively, the first method captures changes in discretized "physical" time, and the second method follows the alterations relative to the network's own tempo of activity. In the following, we analyze the dynamics of LFP patterns using the latter approach, to highlight pattern changes with respect to the hippocampal network's own ebb and flow.

III. RESULTS

We used two groups of mice: "young" (Y) and "old" (O) animals, 2.4 – 3.8 and 7 – 9 months of age respectively, and studied the patterns of their neuronal spiking and principal brain waves. There was significant histopathological difference between old WT and tau hippocampi, but not in young mice, including cortical thinning in old tau mice despite immunohistological confirmation of abundant abnormal tau protein in both young and old tau brains (for details see [25]). On average, it took the mice 15 seconds to traverse the track (Fig. 3A), which included lapsing over the straight segments, turning around the junctions, and pausing at the food wells (Fig. 3B). To capture the dynamics of circuit activity in the context of ongoing behavioral and physiological states, we studied patterns that lasted about $L \approx 2$ sec (thrice shorter than in [21] for improved temporal resolution), which are long enough to produce stable scoring of waveforms and spike trains.

θ -rhythm (4 – 12 Hz) plays major roles in spatial memory, cognition, movement and other phenomena [33–39]. AD-induced alterations of θ -rhythmicity were reported in many studies, based on analyzing instantaneous and averaged parameters of neural activity [40, 41]. We hence inquired whether tau-pathologies also affect the patterning of θ -waveforms, to which end we evaluated their haphazardness (λ_θ) and orderliness (β_θ) scores in both phenotypes, and followed their dynamics.

We noticed two immediate properties in the WT-patterns that are absent in the tau-mice, despite the apparent similarity of their θ -rhythms: 1) coupling between haphazardness of θ^w -waveforms and the animals' speed, and 2) changes of θ^w -patterns between activity and quiescence (Fig. 4A,B). During rapid moves, the stochasticity scores are low, $\lambda_\theta^w = 0.232 \pm 0.001$, $\lambda_\theta^\tau = 0.238 \pm 0.001$, $p < 0.001$, much lower than the Kolmogorov mean ($\lambda^* \approx 0.87$), and $\beta_\theta^w = 1.204 \pm 0.001$, $\beta_\theta^\tau = 1.198 \pm 0.001$, $p < 0.001$, which barely exceeds the minimal value (Fig. 4E). The tiny probabilities

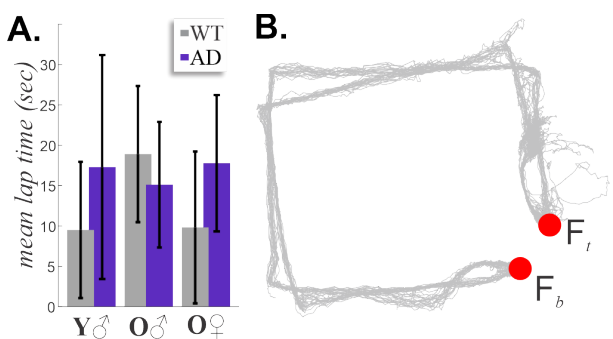


FIG. 3. Locomotion. **A.** No significant difference in the times of lapping from one food well to the other, for all age groups and phenotypes ($p = 0.42$). A typical lap takes young WT males (Y_{σ}^w) 10 sec, young tau-males (Y_{σ}^{τ}) 17 sec, old WT males (O_{σ}^w) 19 sec, old tau-males (O_{σ}^{τ}) 15 sec, old WT females (O_{ϕ}^w) 10 sec, and old tau-females (O_{ϕ}^{τ}) 18 sec. **B.** The gray lines trace the mouse's runs between top and bottom food wells, F_b and F_t (red dots), during one recording session. Behaviorally, inbound trajectories (horizontally aligned quadrilateral) and outbound trajectories (skewed quadrilateral) are different, *e.g.*, the animals tend to turn slowly around the top right corner and dash to F_t , while F_b is approached more leisurely.

of such values (e.g., $\Phi(\lambda \leq 0.23) \approx 8.11 \times 10^{-10}$, $\Psi_{16}(\beta \leq 1.2) \approx 6.74 \times 10^{-4}$, Fig. M1C) show just how rare nearly-periodic patterns are among all possible waveforms. During slowdowns and quiescence, patterns randomize (stochasticity scores grow), as reported in [21].

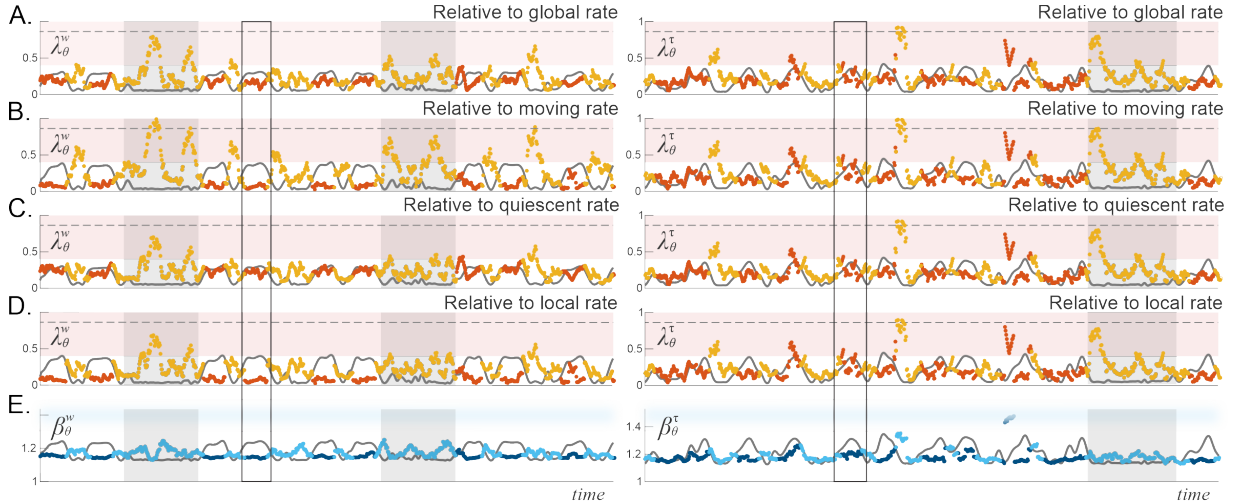


FIG. 4. Haphazardness of θ -waveforms referenced to different physiological contexts. The dark red (λ) and the dark blue (β) points in all panels represent stochasticity scores evaluated during fast-running periods. One such period is highlighted by the vertical black box for each phenotype. The yellow (λ) and the light blue (β) points correspond to slow motions and quiescence. Prolonged quiescence is emphasized by gray-shaded backgrounds. **A.** The λ -score computed relative to the θ -rate averaged over the entire running session, closely follows the animal’s speed (gray trace) during runs and dissociates from it during quiescence in WT mice (left). In tau-mice (right), coupling with speed is weaker. During prolonged quiescence, the θ -patterns randomize: λ -values fall into the generic range, $0.4 < \lambda < 1.8$ (pink stripe same as on Fig. 2B). **B.** λ_θ^w -score assessed relative to the θ^w -rate during active runs shows strict adherence with expected trend during speed ups and increases during slowdowns. In contrast, λ_θ^τ -score for tau-mice appear unaffected by the change in reference. **C.** Relative to quiescence, the adherence of $\lambda_\theta^w(t)$ -dynamics to speed is even tighter than relative to global mean (panel A), while λ_θ^τ -score remains unchanged in both frames of reference. **D.** If θ -rate is assessed relative to movement during movement and relative to quiescence during quiescence, then θ^w -patterns get atypically regular during runs but remain as randomized during quiescence as before, which suggests an unbiased, context-free stochasticity of the latter. Haphazardness of θ^τ -patterns once again remains indifferent to behavior—note the similarity across the right A-D panels. **E.** The β^θ -scores do not depend on the choice of reference behavior.

The θ -patterns’ haphazardness scores discussed above were evaluated relative to the mean oscillatory rates observed over the entire running session, $\bar{n}_\theta^w \approx 8.3$, $\bar{n}_\theta^\tau \approx 8.1$ peaks per second. On the other hand, it is also well-known that not only the amplitude, but also the mean rate of θ -rhythmicity changes noticeably between activity and quiescence. Hence, we inquired how would θ -stochasticity be affected by taking the trending changes into account, and computed two λ -scores: one referenced to the mean rhythm exhibited during active explorations ($\bar{n}_\theta^w \approx 8.6$, $\bar{n}_\theta^\tau \approx 8.5$ peaks per second, Fig. 4B), and the other referenced to the mean oscillatory rate over the quiescent periods ($\bar{n}_\theta^w \approx 7.9$, $\bar{n}_\theta^\tau \approx 8.2$ peaks per second, Fig. 4C), for each phenotype. The results demonstrate that the correspondence between a pattern’s “ongoing haphazardness” and the animals’ speed, reported in [21], is manifested most clearly relative to quiescence. In the “moving frame of reference,” i.e., relative to the rate produced during active moves, λ -scores are low during runs (foreseeably, since now these patterns are expected by design), with the mean value $\bar{\lambda}_\theta^w \approx 0.125$, and grow more

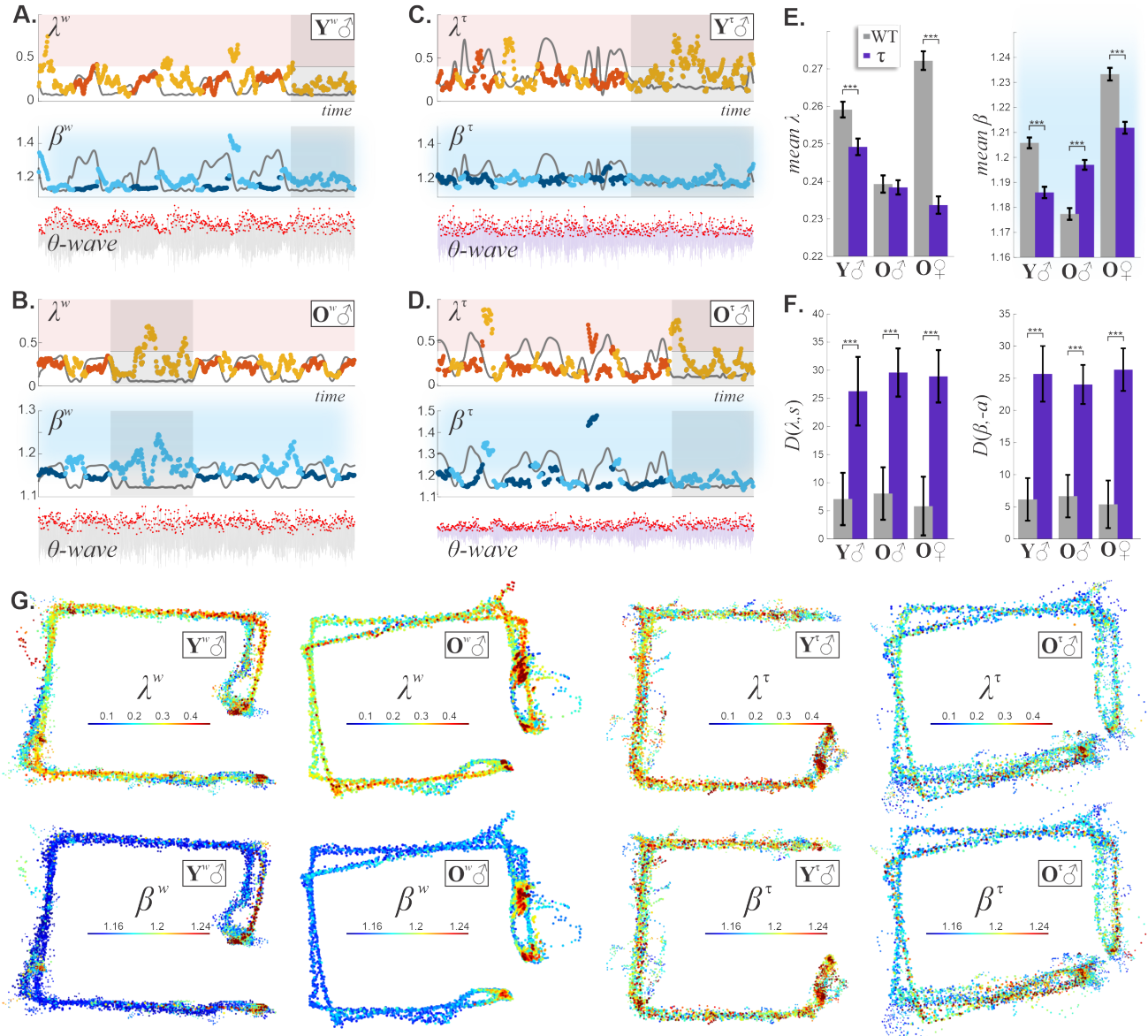


FIG. 5. θ -patterning and AD progression. **A.** During lap running, the haphazardness of θ^w -waveforms in young mice shows coupling to speed (gray line). Prolonged quiescence (gray bands) diversifies θ^w -patterns. The horizontal pink band shows the range of “typical” λ_θ^w -scores, same as on Fig. 2B. The middle panel shows the dynamics of orderliness of θ^w -patterns. Blue stripe outlines the domain of generic β_θ^w -values. During fast moves, θ -waves are close to periodic ($\beta_\theta^w \approx 1.1$) and slightly more disordered during protracted rest. **B.** In the 9-month old WT mice, θ^w -waveforms are similar to those in young mice: quasiperiodic (low β_θ^w), adherent to the mean (low λ_θ^w), coupled to speed during lap running, randomizing during quiescence, and disordering during slowdowns. **C.** In young tau-mice, θ^τ -patterns are more haphazard (higher λ_θ^τ), but strangely, less disordered (β_θ^τ bottom panels) and do not discriminate between the running and the resting states. **D.** Old tau-mice exhibit stronger discordance between θ^τ -patterning and locomotion. **E.** There is a significant difference between the mean λ s in Y_σ^w ($n^w = 5$, $n^\tau = 4$ mice) and O_σ^w ($n^w = 4$, $n^\tau = 5$ mice) cohorts. Orderliness of θ -patterns differs significantly between all animal groups. **F.** LCSS distance between λ_θ and speed, as well as between β_θ and acceleration, is significantly larger in tau-mice. **G.** Healthy mice demonstrate spatial specificity of θ -patterns, consist between laps. In contrast, unsystematic layout of θ^τ -waveforms begins prior to locomotive dysfunction in $Y^\tau\sigma^w$ mice and grows with age (data shown for $n^w = 5$, $n^\tau = 6$ $O^\tau\sigma^w$ animals).

than twice, to $\bar{\lambda}_\theta^w \approx 0.28$, during slowdowns. In other words, relative to quiescence, the faster the animal moves, the less anticipated, more haphazard θ -waveforms s/he generates, whereas relative to activity, such waveforms are stipulated—the chance of cycling squarely at the expected mean rate is vanishing $\Phi(\lambda \leq 0.125) = 2.5 \times 10^{-33}$. Note here that β -scores do not depend on the “reference frame,” i.e., orderliness is always impartial.

In contrast, the hippocampi of tau-mice produce much less structured patterns in both reference frames. Despite some difference in the mean oscillatory rates during active movement and quiescence (8.2 vs. 8.5 peaks per second respectively, Fig. S1), the tau-associated θ -rhythm produces same λ^r -dynamics, whether it is referenced to quiescence or to movement. Unlike the speed-coordinated θ^w -patterns, θ^r -patterns largely ignore the speed dynamics, regardless of reference trend. Even referencing to the ongoing, instantaneous rate reveals no behavioral dependence of the θ^r -stochasticity, which only increase disorder ($\beta^w \approx 1.17$ vs. $\beta^r \approx 1.20$, $p < 0.001$).

This stark contrast with the behaviorally contingent λ -scores of WT mice exposes a curious dissociation of tauopathic network activity from behavior (Fig. 4B-D, right panels). These effects are particularly salient in old animals, which may be due to the net burden on the animal’s physical abilities, as evidenced by lower speed, frequent pausing, etc. (Fig. 5D, [43–45]). However, weakened coupling of θ -waveforms to speed and acceleration are also present in young tau-mice, who do not exhibit locomotive idiosyncrasies (Fig. 5C,D). In fact, there is a highly significant drop of the mean stochasticity scores in all tau-mice’s (except for the haphazardnesses in O_σ mice)—a feature that clearly separates the two phenotypes (Fig 5E).

Similarity between stochasticity dynamics, speed and acceleration can be quantified using the Longest Common Sub-Sequence (LCSS) technique, which allows aligning two profiles through a series of local stretches [46–48]. This measure is robust, as it avoids excessively irregular portions of the data series, is defined in relative terms (percentage difference between the compared functions) and is intuitive. For example, there is no LCSS difference between properly aligned sinusoids, e.g., for $f_1 = \sin(x)$, $f_2 = 2 \sin(x)$ and $f_3 = \sin(2x)$, one gets $D(f_1, f_2) = 0$ and $D(f_1, f_3) = 0$, even with some noise added (Fig. M3A), while combinations of distinct sinusoids exhibit differences (Fig. 6). In other words, LCSS accounts for qualitative, essential mismatches between profiles, ignoring trivial shifts, stretches, and jitters (Fig. M3B).

With this in mind, the mean LCSS separation between the θ -haphazardness and speed, $s(t)$, is twice as large in tau-mice than in WT mice (Fig. 5F). Likewise, the dissimilarity between θ -orderliness, $\beta_\theta^w(t)$, and acceleration, $a(t)$, is about twice larger in tau-mice. In comparison, the Fourier power of the θ -band and its frequency drop by $\sim 27\%$ and $\sim 5\%$ respectively ($P^w = 0.92$ vs $P^r = 0.67$, $p = 0.362$, and $f^w = 8.9$ vs $f^r = 8.5$ Hz, $p = 0.041$, Fig. S5). In other words, changes in θ -patterning are much more expressive than the changes captured by spectral analyses.

Spatial maps of stochasticity are produced by associating the $\lambda(t)$ and $\beta(t)$ scores with the mouse’s ongoing position [21]. As shown on Fig. 5G, healthy mice, both young and old, show

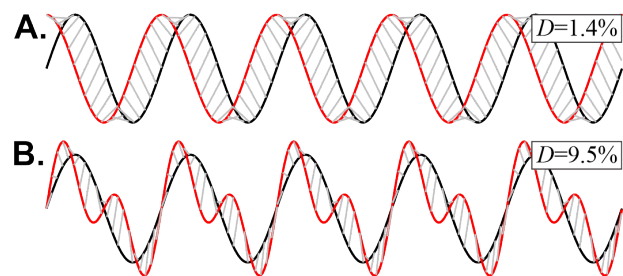


FIG. 6. Locomotion. **A.** LCSS distance between $f_1 = \sin(x)$ and $f_2 = \cos(x)$ is $D(f_1, f_2) = 1.4\%$, which reflects the horizontal adjustments required to match the two sequences. **B.** LCSS distance between $f_1 = \sin(x)$ and $f_4 = \sin(x) + \sin(2x)$ is more than six times higher, $D(f_1, f_4) = 9.5\%$, due to the increased mismatch in the functions’ shapes. Shown is the best match achieved after optimal horizontal and vertical scalings and alignments.

location-specific θ -patterning, reproduced consistently between laps. Close to the food wells, β_θ^w grows, marking a disordering of the θ^w -waveforms, whereas the quiescence-referenced λ_θ^w decreases, indicating that θ^w -wave recovers its expected behavior as the mouse slows down and pauses to eat. Higher λ -values at the corner nearest to the top food well occur as the mouse arrives to F_t , as opposed to when it departs from it, which marks qualitative changes produced at the inactivity onset. Likewise, β_θ^w maps also show higher values as the mouse transitions from movement to quiescence (Fig. 5G). From the quiescence-referenced perspective, patterns randomize further away from the food wells, in the outer expanses of the track, where λ_θ^w increases and β_θ^w drops, indicating the appearance of orderly, but offbeat (relative to reposing expectations) trains of θ -peaks. In either case, the stochasticity maps of WT mice consistently highlight behaviorally significant locations along the animal’s trajectory.

In contrast, old tau-mice lose these properties altogether: both λ_θ^r and β_θ^r become unanchored to the location and scatter arbitrarily along the animal’s path (Fig. 5H). Even the three-month-old tau-mice, who do not exhibit perceptible changes in lap running behavior, already have blurred maps of θ -waveforms, which suggests that tau-disturbance of circuits begins before discernible locomotive abnormalities. These phenomena are even more apparent on the linearized spatial maps (Fig. S6), highlighting the failure of tau-mice to follow the spatial context, which may contribute to spatial cognition and memory dysfunction in the brains of tau mice. In particular, the coupling between λ^w -stochasticity and the speed exhibited by WT mice as they approach the food wells is absent in the tau-mice, which may indicate that the former anticipate forthcoming quiescence and food more than the latter (Fig. S4).

Place cell activity. The space-specific LFP waveforms in WT mice cannot be explained naively via location-specific firing of the hippocampal principal neurons [49, 50]. First, the layout of place cells in the hippocampus is not topographic, i.e., close principal neurons may respond to far-apart place fields, and vice versa, cells with proximate place fields may lie far from each other in the network, and therefore rarely co-contribute to the field detected at a given electrode’s tip [51–54]. Second, although the fields’ layout—the place field map—controls the order of firing, it does not define how the spike trains intersperse, i.e., the overall patterning of spikes arriving from different cells. Furthermore, since place cells’ firing is modulated by the mouse’s location and speed, i.e., is spatially and temporally nonuniform, it is unclear which aspect of a given cell’s spiking should be attributed to its own operational stochasticity, and which part is due to the animal’s behavioral variability. On the other hand, an ensemble of cells, whose fields jointly cover the track, provide a roughly continual spiking flow that allows, *e.g.*, tracking the animal’s position in real time [55–58]. Correspondingly, spike patterning in such a flow can be investigated in the same vein as the series of peaks in waveforms.

We studied ensembles of place cells recorded during a single running session, with place field maps shown on Fig. 7A, and obtained the spike trains’ stochasticity dynamics illustrated on Fig. 7B. Despite the limited number of simultaneously recorded cells, the scores λ_p^w and $\beta_p^w(t)$ recovered in WT mice trace out a tight motif, pointing at a well-defined, dynamic coupling between spiking and locomotion. In other words, spike trains spanning two-second windows (2 – 3 place fields) yield stochastically consistent spike flow, within the limits of generic haphazardness and the orderliness.

When the animal leaves the top food well (note the rapid approaches to F_t along the vertical protrusion), λ_p^w -stochasticity increases to very large values, $\lambda_p^w \approx 10$, which cannot occur by chance ($\Phi(\lambda \geq 10) \approx 0$, Fig. 7B,C). This implies that the spiking trend changes qualitatively, as expected: during runs, place cell firing is triggered by the animal’s physical traversal through the place fields, whereas in quiescence spiking is produced by “offline,” endogenous network activity

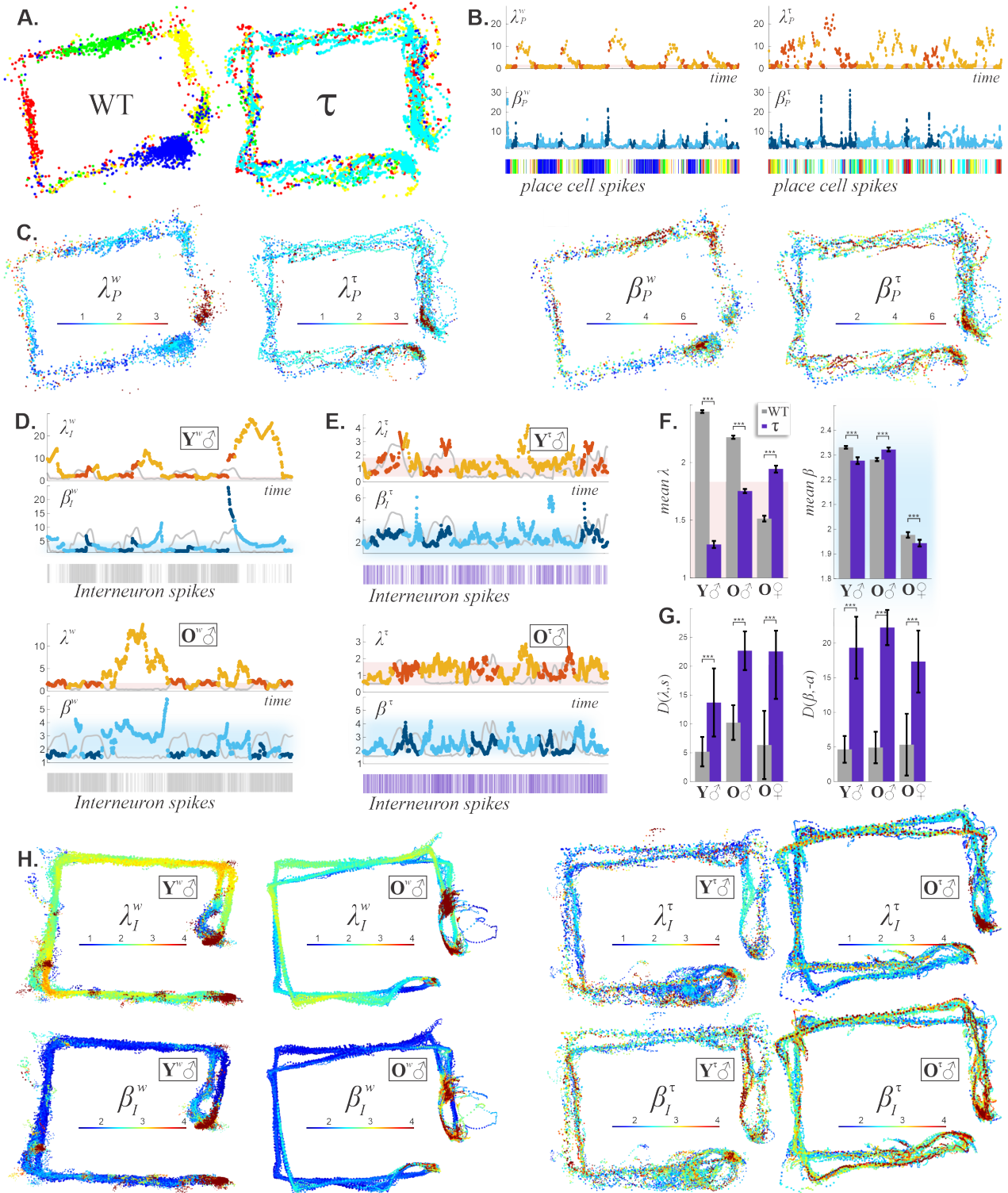


FIG. 7. Spike stochasticity. **A.** Place fields of simultaneously recorded 9-month WT (left) and 9-month tau-mice (right) place cell ensemble jointly cover the track. Each dot represents a spike, color corresponds to a particular place cell, clusters of similarly colored dots represent place fields. The WT-fields are clearly defined, the tau-fields are smeared. **B.** In WT, the combined spike flow produced by the ensemble of all recorded place cells forms a tight motif.

FIG. 7. (continued) The values are stochastically generic at the lower food well, F_b , and along the track itself. At the other food well, the spike trains become deviant and exhibit high clustering ($\beta_p^w \approx 15$), indicating that, at F_t , place cells are engaged in offline, bristle, autonomous activity. These dependencies are not observed in tau-mice, implying that their rapid spiking activity is subdued. Note the greatest upswings of β are dark blue, i.e., occur as the mouse is actively running. Below spike times are marked by vertical streaks, colored as dots on panel A. C. The maps of haphazardness (λ_p , left pair of maps) and orderliness (β_p , right pair) for WT and tau-mice reveal a structural deterioration of place cell activity—segments of generic and atypical spike patterns intersperse throughout the trajectory. D. Haphazardness of interneuronal spike trains in fast running Y_{σ}^w mice is coupled with speed during runs, and rises conspicuously during quiescence ($\lambda_l^w \approx 10$), thus indicating either an implausible-by-chance deviation of firing from the ongoing trend or a trend change. The spike trains (bottom panels) become sparser and cluster more during the rest periods ($\beta_l^w \approx 4$), but then replete and regularize ($\beta_l^w \approx 1$) during active laps. Older WT mice show similar spike patterns, but on a larger scale, from $\lambda_l^w \approx 1.5$ and $\beta_l^w \approx 1$ during running, to $\lambda_l^w \approx 10$ and $\beta_l^w \approx 5$ during quiescence, which suggests that the increase of spiking stochasticity range is likely to be cause by de-tuning. E. In tau-mice, interneurons produce generic spike trains at all times—both λ_l^t and β_l^t are in their respective “typicality bands,” i.e., the ordinance of tau-spiking is akin to random re-shuffling. F. Interneuron spike trains differ significantly between WT and tau-mice, in all demographic groups. G. Regardless of age or sex, the haphazardness and orderliness of WT interneurons responded to behavioral context more than tau-interneurons. H. The spatial patterning of interneuron spike trains in WT mice is modulated by its position. I. Tau-interneurons demonstrate a loss of spatially localized spike patterning

[59–63]. The latter firings include replays or preplays of spiking sequences at a rapid timescale, repeated spiking of individual cells, or a combination these activities, which impact the stochasticity scores [69–76]. Indeed, a replay may last between a couple of dozens to a couple of hundreds of milliseconds, which is comparable to the characteristic interval between spikes triggered by the animal’s physical passing through place fields [60, 64–68]. These brisk, endogenous network activities clutter the overall spike patterns and drive the β_p and λ_p scores up (Figs. 8 and M2). During active movements, the spike disorderliness may also get high, *e.g.*, in the case illustrated on Fig. 7B, $\beta_p^w \approx 5$ as the mouse approaches food at the top arm, which also indicates heightened endogenous network activity.

Tauopathic place cell spiking also changes between generic and cluttering, but it lacks the behavioral specificity of WT place cells. In particular, the occurrences of patterns with atypically high λ_p^t and β_p^t are not tuned to specific physiological states (Fig. 7B), pointing at circuit-level disassociation of collective place cell spiking, both during active behavior and offline [77–79]. Thus, not only the individual tau-cells’ spatial spiking (Fig. 7A), but also the temporal pattern of the ensemble place cell activity is disrupted (Fig. 7B).

The spiking stochasticity maps also illustrate the disruption of place cell ensemble activity in tauopathy (Fig. 7C). In WTs, the distribution of λ_p^w -values is place-specific, with

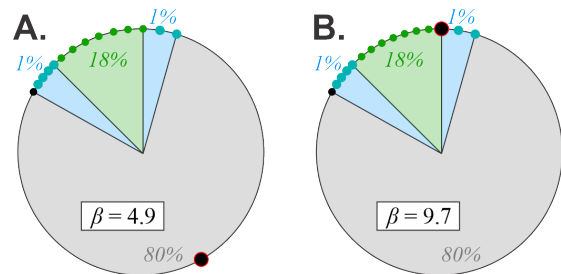


FIG. 8. **Clustering boosts both β and λ .** A. To achieve high values of β , the sequence must cluster. As an example, a unit circle divided into 4 segments covering $Q_i = 1\%, 80\%, 1\%, 18\%$ of the circle, and containing, respectively, $n_i = 2, 2, 4, 7$ uniformly spaced points that jointly produce $\beta = 4.9$. B. By moving a single point from in the sequence from Q_2 to Q_4 (black dot with red outline), β increases to 9.7.

highs and lows occurring in the same positions along the mouse’s trajectory. Curiously, the WT spike patterns also discriminate between the two food wells, exhibiting higher atypicality at one of them. On the other hand, the place cells of tau-mice produce sporadic, stochastically generic patterns anywhere on the animal’s path, and react to both food wells similarly.

Interneurons regulate the hippocampal circuit through inhibition, shaping θ -rhythmicity and other brain waves, in synchrony with the excitatory outputs of principal cells [80–86]. Although the interneurons spike perpetually and at higher frequencies than the θ -waves oscillate (~ 20 Hz vs. ~ 8 Hz), we found their pattern dynamics to be qualitatively similar. First, the haphazardness of interneuronal spike trains, λ_I^w , is clearly coupled to speed, and their orderliness, β_I^w , follows the acceleration (Fig. 7E). Curiously, spike trains visibly sparse out during prolonged rest periods, at which times their scores, λ_I^w and β_I^w , attain very high, improbable values, indicating trend changes relative to active running (Fig. 7D).

Also, the pattern range is wider: during active explorations, spike trains are stochastically generic, unlike the nearly-periodic θ -waves. This suggests that, during lapping, generic interneurons’ spiking contributes to the nearly periodic patterning of θ^w , and during quiescence, clustered spike trains drive spasmodic θ^w -patterns. Note that, since neuronal spiking is coupled to θ -phase, θ -disturbances may in turn randomize spiking.

In contrast, neural stochasticity in tau-mice lingers within typical range, both in activity and in quiescence (Fig. 7E). During the former, the stochasticity dynamics alienates from locomotion ($D(\lambda_I^r, s) \approx 2D(\lambda_I^w, s)$; $D(\beta_I^r, -a) \approx 4D(\beta_I^w, -a)$, Fig. 7G). While the WT mice reproduce interneuronal spiking patterns lap after lap, tau-spikes are largely emancipated from the mice’s position, which by itself may be a source of behaviorally incongruent θ^r -patterning (Fig. 7H). In summary, WT and tau-associated neuronal spikings are manifestly different: the former are location-specific and well-tuned to speed, while the latter are scattered all over the track and generic.

γ -rhythm (30 – 80 Hz) is the second key LFP component that directs information flow in the hippocampal network, controls coupling to sensory inputs, synaptic plasticity, mediates attention, and is involved in a score of other phenomena [87–91]. Previous studies have reported spectral alterations of the γ -rhythms in animal models of AD even before plaque formation [92, 93], and linked aberrant γ -activity to cognitive dysfunction [94]. Indeed, our wavelet scalograms show stronger γ -power (40 – 80 Hz) in WT mice, particularly during periods of active track running between the food wells, while tau-mice do not produce salient γ oscillations (Fig. S5). Pattern analyses allow detailing these differences in much more detail.

To compare γ -waveforms in WT and tau-mice, we extracted patterns of γ -troughs that fit into our selected temporal window, comprised of about $\bar{n}_\gamma^w \approx 59$ and $\bar{n}_\gamma^r \approx 57$ elements. The first observation, compliant with [21], is that γ -waveforms in WT animals are much more variegated than θ -waveforms, as indicated by a wider range of the stochasticity scores (Fig. 9). Relative to quiescence, the γ^w -haphazardness (λ_γ^w -score) consistently co-varies with the speed, while the orderliness, β_γ^w , drops to low values during the fast moves. Thus, as with the θ -waves, γ -rhythmicity in WT mice has distinct running and quiescent dynamics, with different appearances in the two frames of reference (Fig. S7).

Unexpectedly, γ -waveforms in tau-mice show similar behavior: the λ_γ^r -scores also reliably rise and fall with speed, covering about the same range of values, including the periods of prolonged quiescence (Fig. 9A,B). However, tau-haphazardness slightly distances from speed, $D(\lambda_\gamma^r, s^r) \approx 3D(\lambda_\gamma^w, s^w)$, and the orderliness moves farther from the acceleration, $D(\beta_\gamma^r, -a^r) \approx 3D(\beta_\gamma^w, -a^w)$ (Fig. 9D), which may reflect weaker hippocampal coordination of motor effort.

The spatial maps of γ -stochasticity also maintain consistency between laps, in all mice (Fig. 9E). Near the food wells, γ -waveforms in both WT and tau-mice assume shapes typical for

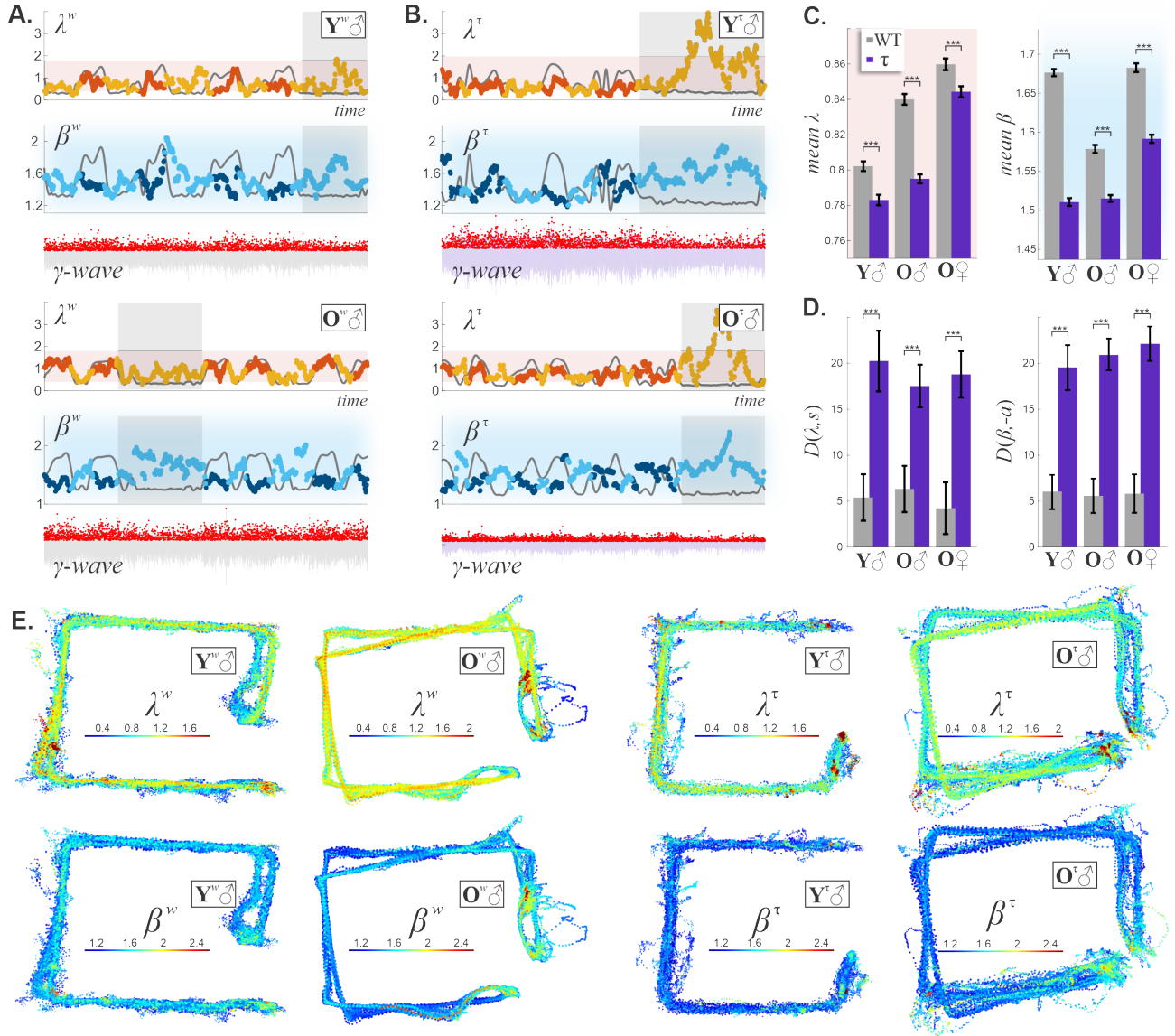


FIG. 9. γ -waveform dynamics. **A.** In WT mice, γ^w -waveforms are, for the most part, stochastically generic, constrained within the typicality zones, but more diverse than the θ -waveforms (wider λ_γ - and β_γ -ranges). During active explorations, γ^w -patterns in Y° mice show coupling to speed (gray trace) and complex dynamics during quiescence (gray bands). $\beta_\gamma^w(t)$ -scores show that γ^w -waves are close to periodic during activity and disorganize during quiescence, especially at the food wells. **B.** Surprisingly, in tau-mice, the dynamics of γ -stochasticity is similar: haphazardness of γ^τ -troughs is also coupled with speed and elevated during quiescence. The orderliness, $\beta_\gamma^\tau(t)$, likewise, drops during runs and rises to generic levels, $\beta^\tau \approx 2$, when s/he stalls. **C.** Mean λ_γ and β_γ are significantly lower in tau-mice, in all groups—once again, subdued stochasticity is a signature of tauopathy. **D.** The LCSS difference between haphazardness and speed (left) and between orderliness, β_γ^w , and acceleration (right) in WT mice, is more than twice smaller than in tau-mice. **E.** Spatial maps show similar lap-consistent patterning of WT (left panels) and tauopathic (right panels) γ -rhythms.

quiescence, despite heightened disorder in this area (smaller λ_γ^x , bigger β_γ^x values). Conversely, series of γ -troughs consistently become more haphazard and yet more orderly (take nearly-sinusoidal forms), as the mouse rounds the track's corner furthest from the food.

Relative to the fast-moving mean, the story can be retold as follows: during runs, γ -waveforms

tightly match with the pseudoperiodic moving trend (λ_y^x drop), and during extended rest they scramble (λ_y^x rises, Fig. S7B). In tau-mice, γ -waveforms show similar behavior-specific alterations, albeit more subdued than their WT littermates. The λ -maps further emphasize the dichotomy of γ -patterns between movement and quiescence.

The fact that θ -waveforms in tau-mice are affected more than γ -waveforms also implies that neuropathology weakens coherence of θ - and γ -patterning. A number of studies based on correlative analyses of θ - and γ -waves' instantaneous amplitudes, frequencies and phases [95–97], show that physiologically functional θ/γ -comodulation in WT animals [98, 99] gets disrupted at early stages of AD [92, 100, 101]. Our results show similar effects at the level of patterns: the LCSS distance between θ - and γ -haphazardness, $D(\lambda_\theta, \lambda_\gamma)$, are significantly larger in tauopathic than in WT mice (Fig. S8A). Curiously, the differences between speed and θ - and γ -haphazardness are comparable in WT mice of all ages and sexes, whereas in the older tau-mice, speed is weaker coupled to θ^τ - than to γ^τ -waveforms, suggesting that θ^τ/γ^τ decoupling is due to deterioration of the former.

Ripple events (R) are perturbations of the high-frequency (150 – 250 Hz) extracellular field oscillations, which reflect the dynamics of autonomous activity in the hippocampal network [102–105]. For example, R are known to co-occur with replays and preplays, which indicates a connection with memory processing and offline cognitive activity [62, 63, 106–111]. Several mouse models of AD show disruptions of hippocampal rippling, including increases and decreases of ripple frequency, amplitude, phase alterations, as well as disrupted temporal profile, and even disappearance of the Sharp Wave Ripple (SWR) events [66, 77, 112, 113]. Yet, the overall structure of the LFP's high frequency domain, as captured by wavelet and Fourier transforms, are fairly comparable between both phenotypes (Fig. S9), whereas pattern-level differences are distinct.

To evaluate these differences, we identified “splashes” of the ripple waves' (amplitudes that exceeded two standard deviations from the mean) and selected series of these events that fall within our selected time window¹. The resulting R patterns contained, on average, a similar number of items in WT and tau-mice ($\bar{n}_R^w \approx 14$ and $\bar{n}_R^\tau \approx 16$ respectively², Fig.S3).

In accordance with [21], the range of WT stochasticity scores referenced to quiescence is wide, encompassing both strongly deviating and overly compliant patterns (Fig. 10A). The haphazardness of rippling in healthy mice, λ_R^w , exhibits clear coupling with speed (Fig 10A,D), and counter-phase coupling with acceleration. At high speeds, R^w series are nearly periodic, $\beta_R^w \approx 1$, and range from nearly-periodic to clustering ($\beta_R^w \gtrsim 4$) during quiescence. In contrast, tau-mice exhibit a smaller assortment of rippling for all age and sex groups ((narrower range of β_R^τ and λ_R^τ , opposite to spikes, Fig. 10B,C), and more than twice weaker coupling between orderliness and acceleration (Fig. 10D). Additionally, λ_R^w is sensitive to changes of reference trend, while the tauopathic rippling patterns are indifferent to cross-referencing (Fig. S10). This loss of coherence between R^τ -patterning and physiological state, speed or acceleration, suggests that functionality of rapid network dynamics is also compromised or lost in tauopathy: tau-rippling is akin to sluggish responding to random disturbances (generic-lowish λ_R^τ), whereas WT ripples are driven by targeted activity (Fig. 8).

In terms of spatial maps, both young and old WT mice show clear lap-dependent R -patterning as well as a higher diversity of patterns at the food wells, while tau-mice ripple impartially, with scores deviating sporadically from the background (Fig. 10E,F, S10).

¹ Note that the 2σ -criterion for selecting R is much lower than the one used in SWR detection (typically $5 - 7\sigma$), which allows identifying R in tau-mice of both age groups.

² Note similarity with the θ -peak numbers.

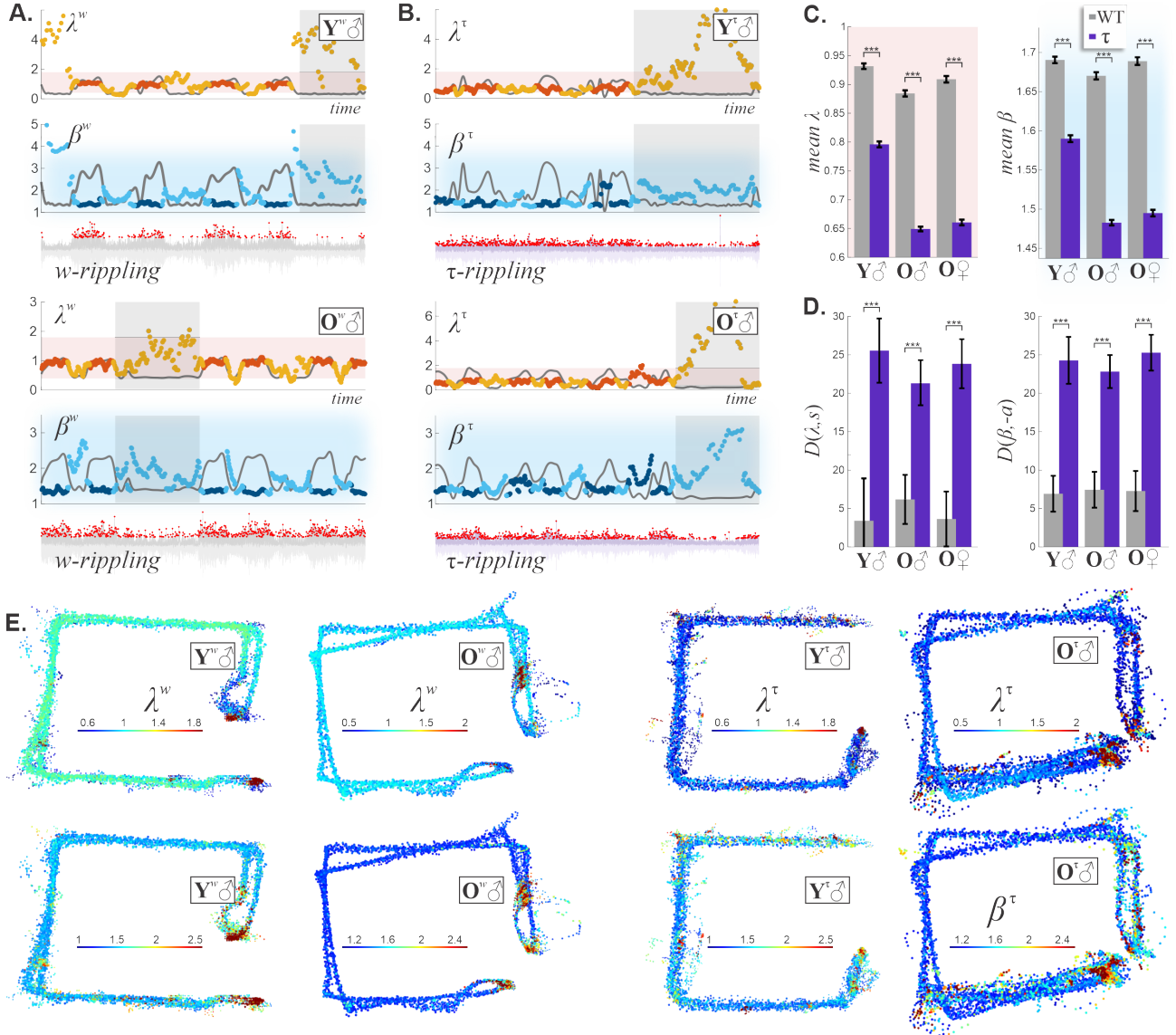


FIG. 10. Ripple event stochasticity. **A.** The haphazardness of R -patterns in young WT mice (top panel) and old WT mice (bottom panel), is trending during inactivity and scrambles during runs, in a speed-coupled manner. The disorder is also high during quiescence ($\beta_R^w \geq 2$), and nearly periodic during movement ($\beta_R^w \approx 1$ at maximal speed). (continued) **B.** In tau-mice, R -patterns do not distinguish between moving and quiescent states, and are uncoupled from speed. Additionally, both orderliness and haphazardness remain much lower than in WT's and do not get atypical, indicating that tau-rippling is stochastically uneventful and unresponsive to moves or quiescence. **C.** WT R^w -patterns produce significantly higher λ - and β -scores, indicating a much wider range of patterns compared to tau-mice. **D.** On average, speed is twice closer to λ_R^w than to λ_R^τ , and acceleration is twice closer to β_R^w than to β_R^τ . **E.** Spatial maps of λ_R^w and β_R^w for both young and old mice reveal spatially specific patterning of R . In contrast, spatially scattered λ_R^τ - and β_R^τ -values indicate disorder and varied patterns throughout and between laps.

IV. DISCUSSION

Most studies focus on cellular AD pathologies or the associated cognitive changes, whereas circuit-level mechanisms of neurodegeneration receive less attention [1–3]. This is partly explained by the immense complexity of the hippocampo-cortical network, intricacy of its dynamics, and multitude of external inputs, which render detailed, deterministic, causal connections nearly intractable. Furthermore, understanding the mechanisms by which the individual neurons and synapses contribute to large-scale phenomena, such as the rhythmicity of extracellular fields, is complicated due to the preponderance of collective, emergent effects, such as spontaneous synchronization [114–118]. Additionally, concurring neuronal dynamics have different origins and functions. For instance, θ -rhythms are generated by medial septal inputs and local interactions between interneurons and principal cells [42, 119], whereas γ -rhythms are produced via local ensemble activity and perisomatic inhibition [103, 120].

Remarkably, despite the differences in spatiotemporal scales, mechanisms and implementations, patterns of neural activity follow the same universal statistics described by Kolmogorov and Arnold distributions. In other words, the mathematical laws governing the probability of patterns' appearance overrides the exhaustive physiological details, much like the sampling distribution of the means is always Gaussian, irrespective of the mechanisms that contribute individual inputs (Fig. 11). Consequently, time-variations of stochasticity scores, $\lambda(t)$ and $\beta(t)$, evaluated for continuously evolving waveforms and spike trains provide an impartial description of the circuit dynamics, emancipated from the minutiae.

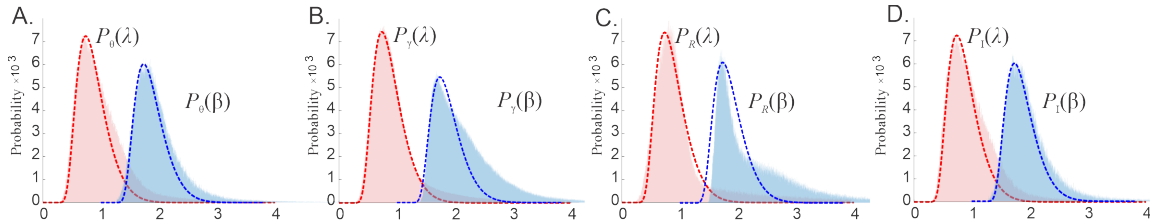


FIG. 11. Statistical universality of patterns. Normalized histograms of haphazardness (λ , pink) and orderliness (β , blue), evaluated for 1,000,000 of 25-point sequences of: **A.** θ -peak fluctuations; **B.** γ -peaks; **C.** ripple events; **D.** interneuronal spikes. Dashed lines show the shapes of the theoretical Kolmogorov and Arnold distributions, scaled to the histograms' heights. These results demonstrate, first, that the varieties of waveforms are broad enough to capture the distribution's ranges and shapes in both WT and tau-mice. Moreover, these distributions hold true regardless of data source (i.e. phenotype, age, LFP, single neuron, etc.). In the case of γ -patterns and ripples, β_γ and β_R histograms deviate from the impartial β -statistics, due to larger proportions of cluttering waveforms. Data collected from 14 WT and 16 tau-mice, the spikes are recorded from 12 WT and 5 tau-interneurons.

An important advantage of the λ/β stochasticity scoring is its intuitive transparency, that enables reasoning about neural activity in colloquial terms, focusing on structural regularities or peculiarities, *e.g.*, atypical periodicity, excessive clustering, etc. Due to their universality, these quantities may potentially be actualized, i.e., represented explicitly in the brain, and used to guide system-level information exchange, movement coordination, memory encoding, retrieval and other phenomena.

Returning to the phenotype comparisons, generic differences between tau pathology and WT cases can be summarized as follows. While healthy mice exhibit well-tuned, purposeful, behavior-modulated LFP rhythmicity and spiking patterns, tau-mice show dissociation of neural activity from physiological and behavioral states. The way in which the hippocampal spiking is produced,

modulated by the brain waves and imparted onto downstream networks is qualitatively altered by tau-pathology.

These observations are in line with previous studies demonstrating that compromised coupling between LFP rhythms and locomotion, loss of spatial and temporal fidelity of hippocampal neurons are key contributors to learning and memory impairments [100, 101, 121, 122]. We demonstrate that not only do tau-pathologies disturb individual neurons and rhythms, but they also scramble the overall spatiotemporal architecture of the hippocampal activity, which is saliently manifested. The morphological alterations illustrated on Fig. 1 may indeed be indicative of systemic alterations in circuit activity and can hence serve as signatures of neurodegeneration.

V. ACKNOWLEDGMENTS

C.H. and Y.D. are supported by NIH grant R01AG074226 and R01NS110806, and by NSF grant 1901338. C.J. and D.J. are supported by NIH grants R01MH112523 and R01NS097764.

VI. MATHEMATICAL SUPPLEMENT

Computational algorithms are based on the works [26–29, 123–125], and outlined in [21].

1. *Kolmogorov score.* Let $N(X, L)$ be the *empirical distribution* of an ordered sequence $X = \{x_1, x_2 \dots x_n\}$ —the number of x -elements in the interval between 0 and L ,

$$N(X, L) = \{\text{number of } 0 \leq x_k < L\}.$$

For semiperiodic series, *e.g.*, brain rhythms and regularly appearing spikes, this function grows proportionally to L , with the mean slope defined by the average frequency, $\bar{N}(X, L) = \bar{f}L + m$. The deviations of a pattern X from this mean, normalized by a “random walk” magnitude,

$$\lambda(X) = \sup_L |N(X, L) - \bar{N}(X, L)| / \sqrt{n}, \quad (1)$$

is universally distributed. The probability distribution

$$P(\lambda) = 2\lambda \sum_{k=-\infty}^{\infty} (-1)^{k+1} k^2 e^{-2k^2 \lambda^2}, \quad (2)$$

is concentrated between $\lambda^- = 0.4$ and $\lambda^+ = 1.8$, with the mean $\lambda^* \approx 0.87$ (Fig. 2B). Outside of these limits, λ -scores appear with probability less than 0.3%, marking the “atypical” patterns [26–29, 125]. Including higher-order corrections to the Kolmogorov score,

$$\lambda(X) \rightarrow \lambda(X) \left(1 + \frac{1}{4n}\right) + \frac{1}{6n} - \frac{1}{4n^{3/2}}, \quad (3)$$

increases statistical accuracy for short sequences (10 – 20 elements) to over 0.01% [126, 127].

2. *Arnold score.* Arranging the elements of X on a circle of length L yields n consecutive arcs, with lengths l_1, l_2, \dots, l_n (Fig. 2C). The combination

$$\beta = \frac{n}{L^2} (l_1^2 + l_2^2 + \dots + l_n^2) \quad (4)$$

quantifies the orderliness of X : if the points x_k “repel” each other and strive to maximize separation, then β is small (minimum $\beta = 1$ is achieved by perfectly symmetrical, equispaced layouts). If the elements attract and tend to cluster, then β is large (up to $\beta = n$, reached when all x_k s collapse into one point). Randomly placed, independent elements produce β -scores close to the universal value, $\beta^* \approx 2$ [123, 124]. The length L of the circle was selected so that the distance between the end points, x_0 and x_n , on the circle became equal to the mean of the remaining arc lengths, $l_n = |x_n - x_0|_{\text{mod } L} = \bar{l}_i$.

3. *Probability β -distributions* are parameterized by the number of elements in the sequence. As shown on Fig. M1, these distributions have the mean of $\beta_n^* \approx 2n/(n+1)$ and a close-by peak, and rapidly decay as β approaches $\beta_{\min} = 1$ or grows over $\beta^+ = 3.5$. For intermediate sized samples used in practice, *e.g.*, for $n = 50$, $\beta^- = 1.5$ and $\beta^+ = 3.2$ (Fig. M1D).

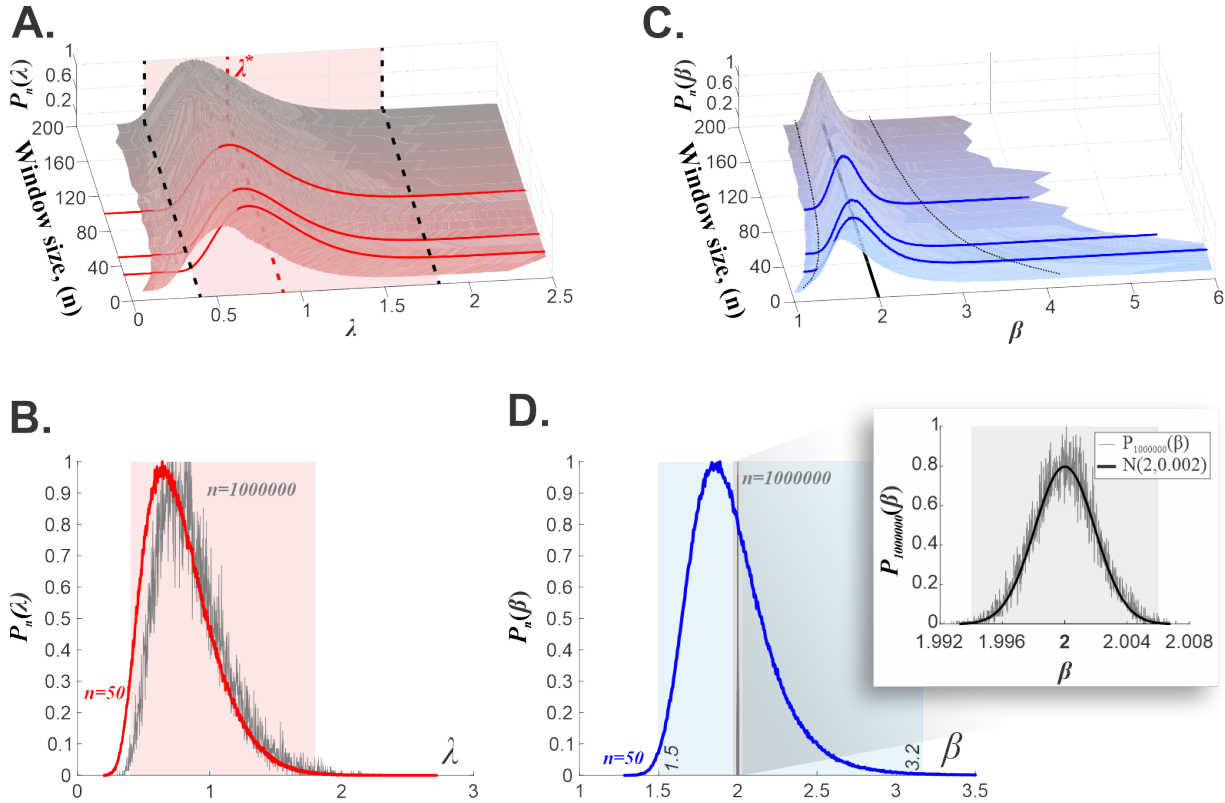


FIG. M1. Stochasticity scores and sample sizes. **A.** The shape of the λ -histogram depends weakly on the sample size. If the latter exceeds $n \approx 25$, the histogram closely matches the theoretical shape (2). The shadowed domain contained between dashed lines contains 99.7% of values. **B.** Empirical λ distributions for a 50-point sample (red) compared to a 1000000-point sample (gray) reveals little difference. **C.** β -distributions narrow as the number of samples per window increases. The dashed lines in the horizontal plane ($n - \beta$ axes) mark the upper and the lower bounds, β_n^+ and β_n^- , which contain 99.7% of β -values for each sample size. Shown are the β_n -histograms numerically evaluated for $20 \leq n \leq 200$. In terms of the relative size, $x = n/200$, the polynomial fits for the limiting curves produce $\beta_x^+ \approx 4.5 - 8.4x + 16x^2 - 15.2x^3 + 5.44x^4 + O(x^5)$, with $R^2 = 0.9994$ and $\beta_x^- \approx 1.1 + 2.2x - 4.0x^2 + 3.92x^3 - 1.42x^4 + O(x^5)$ with $R^2 = 0.9995$. **D.** Comparing β distributions for a 50-point sample with typical range (shadowed blue) to the empirical distribution of 1000000-sample sequences (gray) reveals significant narrowing. The pop-out represents the zoomed-in very narrow 1000000-point β -distribution, approximated by a Gaussian distribution with mean 2 and standard deviation 0.002 (black line).

4. *Rapid replays increase λ and β .* A dense sequence of points creates a “bulge” in the empirical distribution, hence resulting in a λ that deviates farther from the expected mean (Fig. M2A). Similarly for the orderliness: if n points are distributed uniformly on the circle, $l_k = L/n$, $k = 1, 2, \dots, n$, then $\beta = 1$. If one arc is additionally split by $m - 1$ extra points into m smaller equal arcs of lengths $\tilde{l}_i = L/nm$, $i = 1, 2, \dots, m$ then

$$L = \sum_{k=1}^{n-1} l_k + \sum_{i=1}^m \tilde{l}_i,$$

and (4) produces

$$\beta = \frac{(n-1) + m}{L^2} \left(\sum_{k=1}^{n-1} l_k^2 + \sum_{i=1}^m \tilde{l}_i^2 \right) = \frac{n+m-1}{n} \left(\frac{n-1}{n} + \frac{1}{nm} \right). \quad (5)$$

As an illustration, if $m = 1$ (no points added), then $\beta = 1$. If $m = n + 1$, then (5) reduces to

$$\beta = 2 \frac{n}{n+1}, \quad (6)$$

which, coincidentally, matches the ‘‘impartial mean’’ β^* [123, 124]. If $m = 2n + 1$, then formula (5) yields

$$\beta = 3 \left(1 - \frac{2}{2n+1} \right), \quad (7)$$

and if $m = n/2 + 1$ (assuming n is even), then

$$\beta = \frac{3}{2} \left(1 - \frac{1}{n+2} \right),$$

etc. In general, if p arcs, $l_{k_1}, l_{k_2}, \dots, l_{k_p}$, are subdivided by additional $m_1 - 1, m_2 - 1, \dots, m_p - 1$ points, uniformly laid out, they yield, respectively, m_1 sub-arcs of length $\tilde{l}_{k_1} = L/(nm_1)$, m_2 sub-arcs of length $\tilde{l}_{k_2} = L/(nm_2)$ and so forth. Correspondingly,

$$\begin{aligned} \beta &= \frac{(n-p) + m_1 + \dots + m_p}{L^2} \left(\sum_{k \neq k_j} l_k^2 + \sum_{i_1=1}^{m_1} \tilde{l}_{i_1}^2 + \dots + \sum_{i_p=1}^{m_p} \tilde{l}_{i_p}^2 \right) \\ &= \frac{n + m_1 + \dots + m_p - p}{n^2} \left(n - p + \sum_{j=1}^p \frac{1}{m_j} \right). \end{aligned} \quad (8)$$

By varying proportions between m_j and n , changing the number of divided segments, etc., one can produce different values of β to model clustering densities discussed in Sec. III, as illustrated below.

Case 1. If the number of extra points on l_{k_j} is $m_j = n + 1$, then (8) reduces to

$$\beta = (p+1) \left(1 - \frac{p}{n(n+1)} \right), \quad (9)$$

i.e., each split segment contributes $\Delta\beta \approx 1$ to raising the overall β , as implied by (6).

Case 2. If there are $m_j = 2n + 1$ points in each divided segment, then (8) yields

$$\beta = (2p+1) \left(1 - \frac{p}{n(2n+1)} \right), \quad (10)$$

i.e., the effect described by (7) is produced p times.

If the sliding window contains N data points total,

$$N = n - p + \sum_{j=1}^p m_j,$$

then one gets $N = n(p+1)$ in Case 1 and $N = n(2p+1)$ in Case 2. Specifically, if $N = 15$ with the θ -peaks or ripple events, then $15 = n(p+1)$ and $15 = n(2p+1)$. With two inserted subsequences, $p = 2$, the first equation necessitates $n = 5$ regular points, and the second $n = 3$ points, yielding $\beta = 2.85$ (Eq. 9) and $\beta = 4.5$ (Eq. 10).

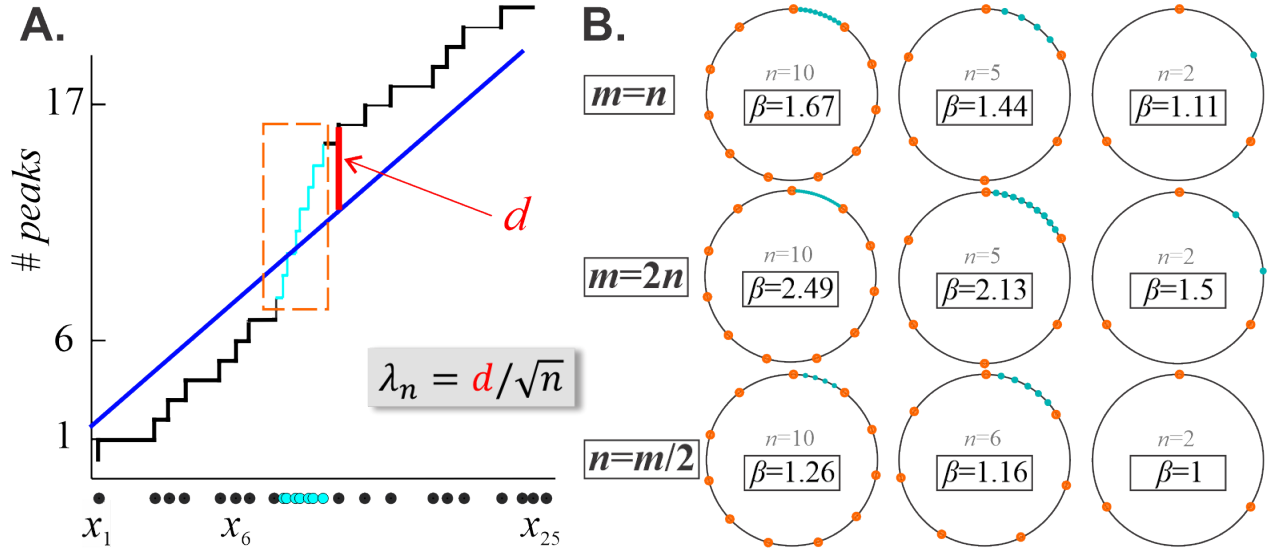


FIG. M2. **Clustering segments increase stochasticity scores.** **A.** The empirical distribution built for a sequence of 17 points (Fig. 2A), with additional seven points inserted (blue segment of the staircase). The latter raises the intercept without altering significantly the slope of the mean (blue line), which results in a jump-up of haphazardness score, λ . **B.** The circle is partitioned into $n + 1$ equal arcs, with one further split into m segments. Varying the values of n and m , or adjusting the proportion of each, produces “clustering” that affects the value of β .

4. *Longest common subsequence.* Comparing shapes is a challenging problem. Computing point-by-point Euclidean distances may produce misleading results, especially when signals contain noise or if there are misalignments between pairs of points. More intuitive results are produced by nonlinear alignments that allow for elastic shifting of points without rearrangement, *e.g.* longest common subsequence (LCSS) [46–48].

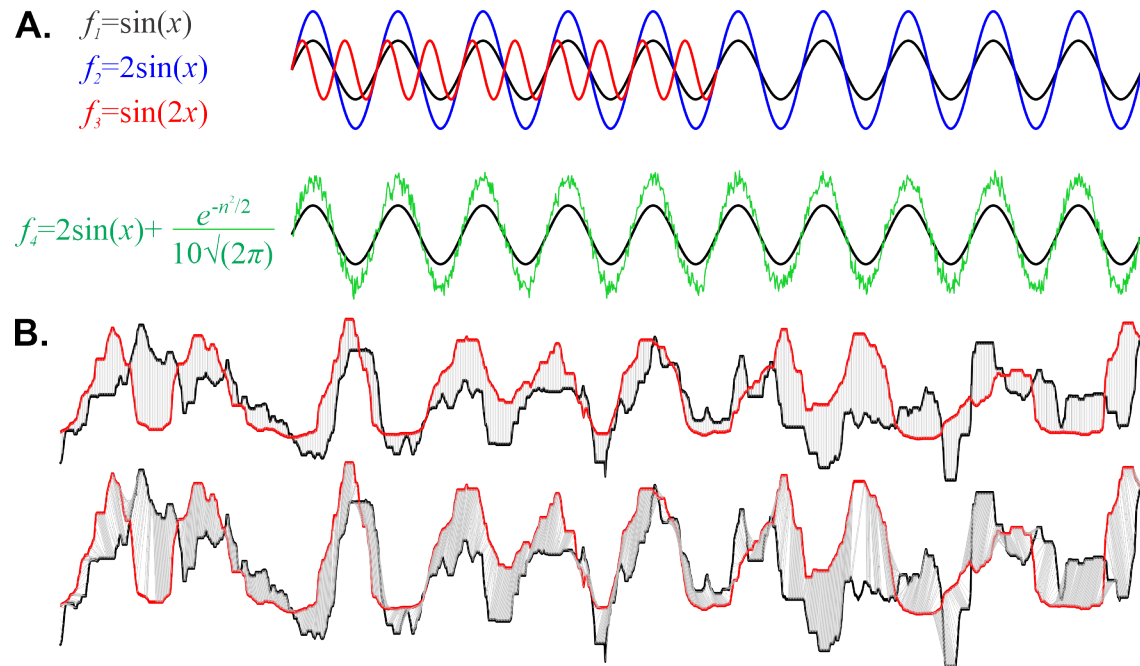


FIG. M3. **LCSS example.** **A.** LCSS discounts shifts or amplitude changes (top), as well as added noise—in all illustrated cases the LCSS distance vanishes. **B.** Euclidean distance for vertical point-to-point matching on example λ vs speed data can result in poor shape comparison. **C.** Oblique LCSS matching (top) allows shifting of the time axis for more intuitive comparisons of the speed vs λ profiles. The bottom panel shows the LCSS matched shapes.

VII. SUPPLEMENTARY FIGURES

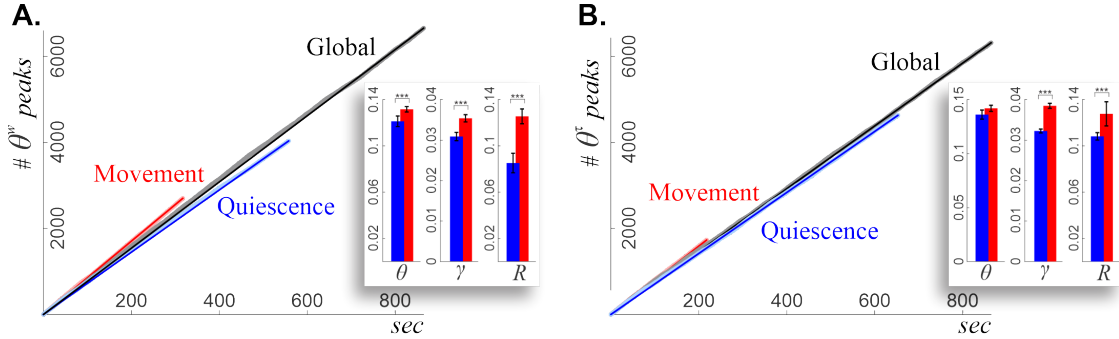


Fig S1. **Brain wave trends.** Brain waves are oscillatory in nature, producing linear trends which can be used as the basis for calculating λ . For example, the θ wave produces peaks that appear at frequency ≈ 8 Hz. However, the behavior of the animals may situationally affect the expected patterning of brain rhythms. Correspondingly, computing λ relative to specific means, i.e. for different physiological contexts, allows gaining a comprehensive understanding of data haphazardness. **A.** Globally averaged WT θ -cadence amounts to approximately 8 Hz. Yet, this value changes in quiescence and in movement. The insert reveals significant differences in the θ , γ , and R trends between movement and quiescence. **B.** Brain wave frequencies of tau-mice also discriminate between activity and rest. Note that these differences are diminished in R and are eliminated in θ .

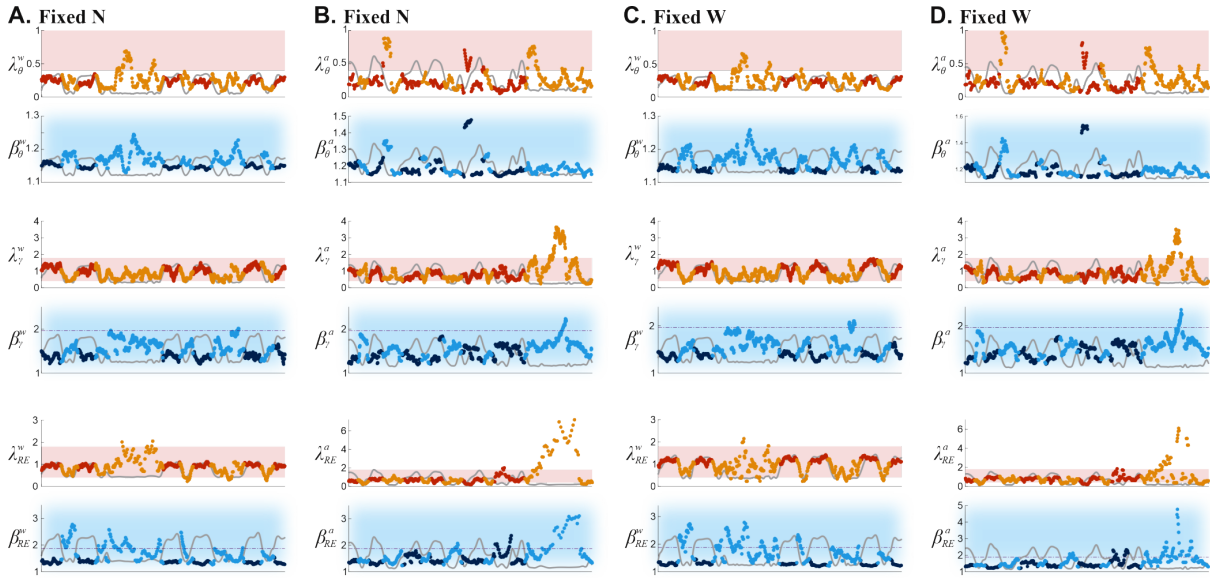


Fig S2. **Fixed number of peaks per window versus fixed window size.** This figure illustrates the difference in stochasticity dynamics evaluated using a fixed number of peaks per window as compared to fixed time windows. **A.** Time window of fixed width, n , for WT mice. $n_{\theta}^w = 16$, $n_{\gamma}^w = 59$, and $n_R^w = 15$ peaks. **B.** Time window of fixed width, n , for tau-mice. $n_{\theta}^{\tau} = 16$, $n_{\gamma}^{\tau} = 57$, and $n_R^{\tau} = 15$ peaks. **C.** Fixed time step, L , for WT mice. $L = 2$ sec for all waves. **D.** Fixed time step, L , for tau-mice. $L = 2$ sec for all waves.

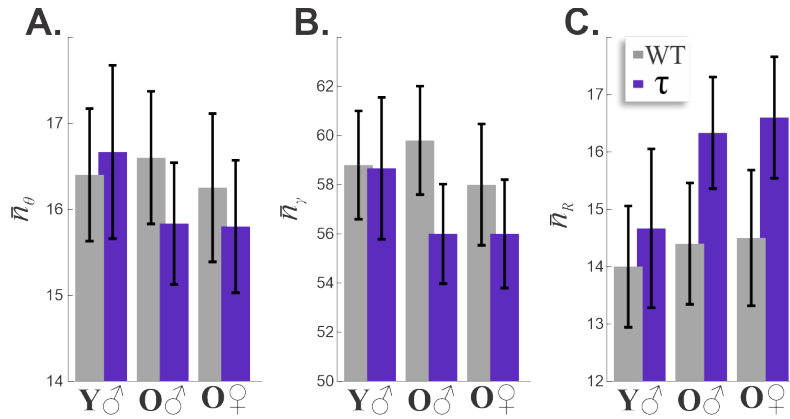


Fig S3. Average number of peaks in each wave, per two second window is similar for all ages and phenotypes. There were on average $n_\theta = 16.2$ peaks of the θ -wave (panel A), $n_\gamma = 57.8$ peaks of γ (in panel B), and $n_R = 15.2$ peaks (panel C) per window.

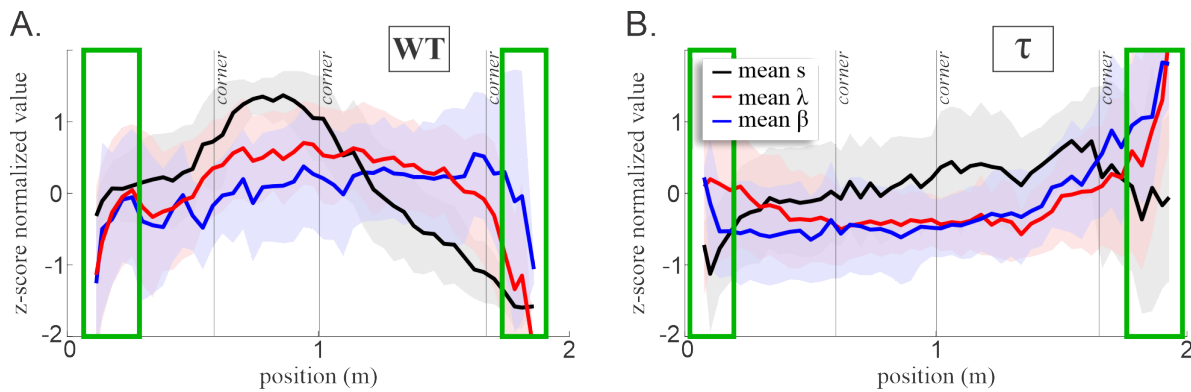


Fig S4. Mean stochasticity and speed along the mice's linearized trajectory, with the corner locations demarcated by vertical lines. Standard deviations for all variables (color-coded) are represented by the shaded bands around the corresponding means. The speed and the λ/β -values for each lap were normalized by z-score and averaged. **A.** WT mice produce LFP patterns that are not only consistent between laps, but also appear to trend with the animals' speed. Note that λ , β , and speed correlate at the ends of the trajectory (green boxes). **B.** tau-mice scores, λ^τ and β^τ may oppose the speed, increasing at food wells while speed decreases, and vice versa (green boxes).

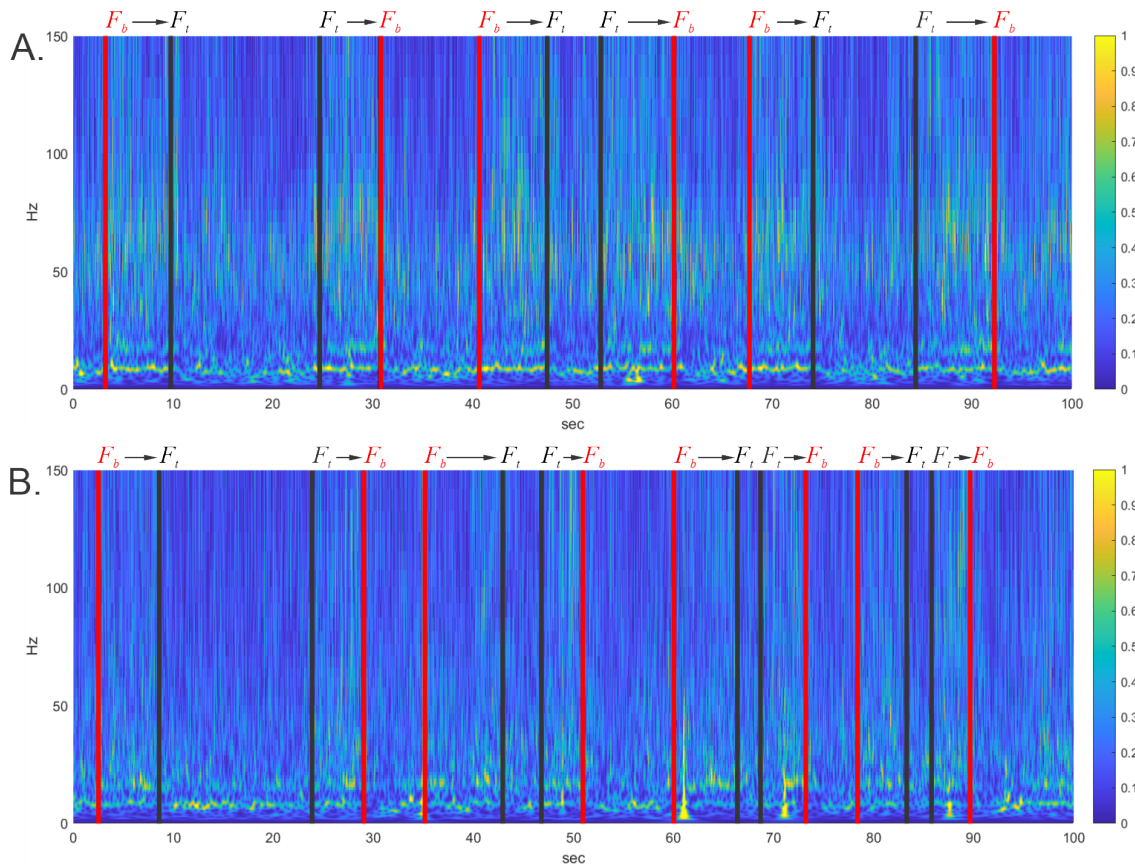


Fig S5. **Continuous wavelet transform** of LFPs recorded from WT and tau-mice (panels **A** and **B**). Red lines marked by “ F_b ” correspond to the bottom food well, and the black lines marked by “ F_t ” represent the top food well on Fig. S6. The spectrogram reveals minor changes in the power of the LFP frequencies as the mice change between active movement and quiescence, whereas pattern differences are dramatic (Figs. 5, 9, 10).

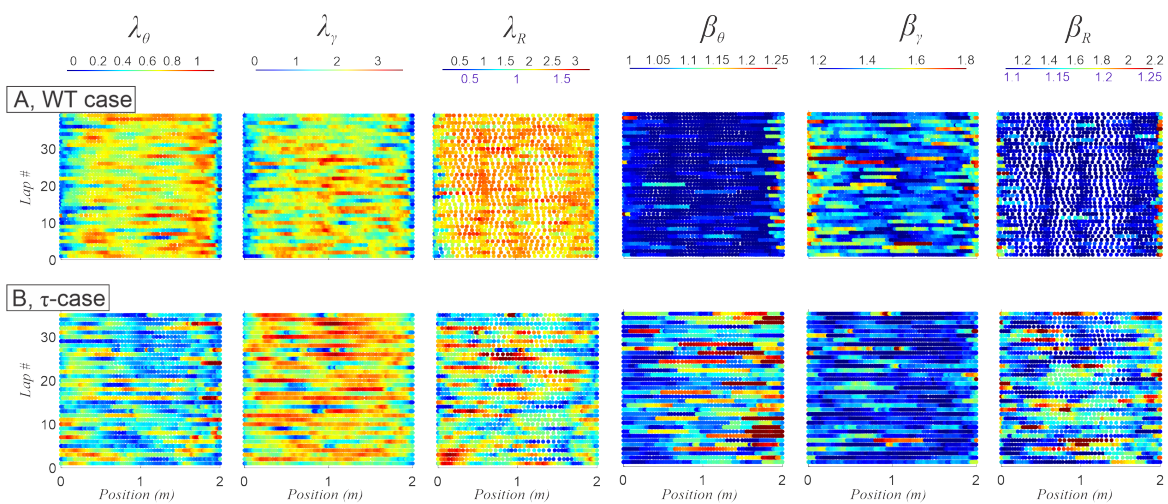


Fig S6. **Linearized spatial stochasticity map of brainwaves by lap**. **A**. The θ , γ , and R maps show consistent structures between laps in healthy mice. **B**. In tau-mice, maps are shuffled and spatial organization is lost.

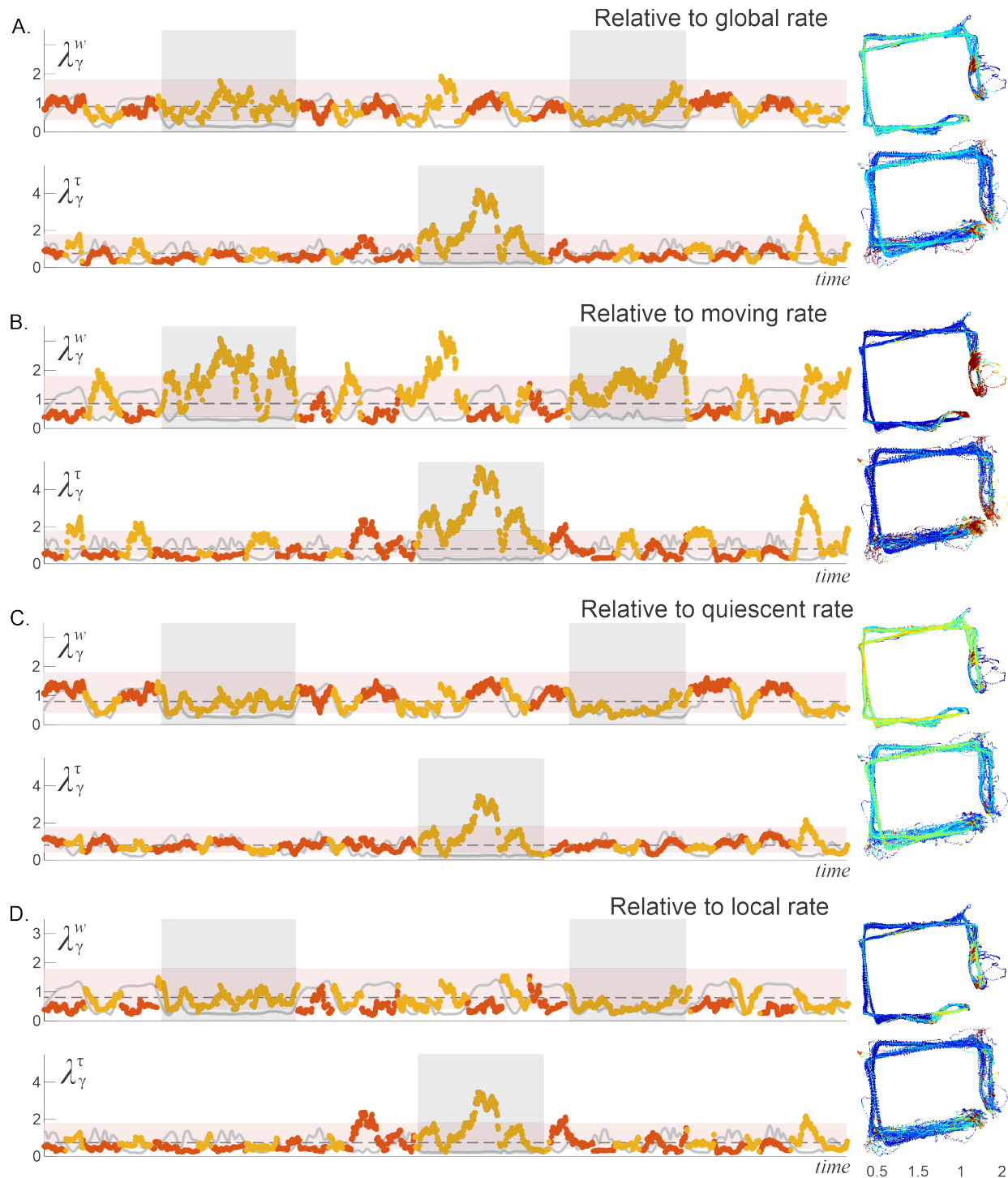


Fig S7. Haphazardness of γ -wave referenced to different physiological states in WT and tau-mice. **A.** Relative to the global average, γ -rhythms are more stochastic than θ -patterns. λ -scores for WT (top) and tau (bottom) falls within the pink “typicality” zone. Nevertheless, γ -patterns are sensitive to changes between movement and quiescence, rising during runs and falling during brief pit-stops at the food wells. λ_γ -maps on the right reveal similar spatial organization in both phenotypes. **B.** Relative to the active track running, λ_γ drops to atypical values during movements, indicating the designed (hence stochastically abnormal) adherence to the chosen trend, as well as rises to atypically high values during periods of prolonged quiescence. This is another “statistical perspective” on the qualitative differences between γ -cadence during quiescence and activity. Note the arrangement of the corresponding low and high λ -values on the spatial λ maps (right). **C.** Relative to quiescence, λ_γ tends to follow the profile of speed. **D.** Relative to the ongoing trend, λ_γ remains low. **E.** β_γ for WT and tau-mice shown for reference. Compare this to Fig. 4.

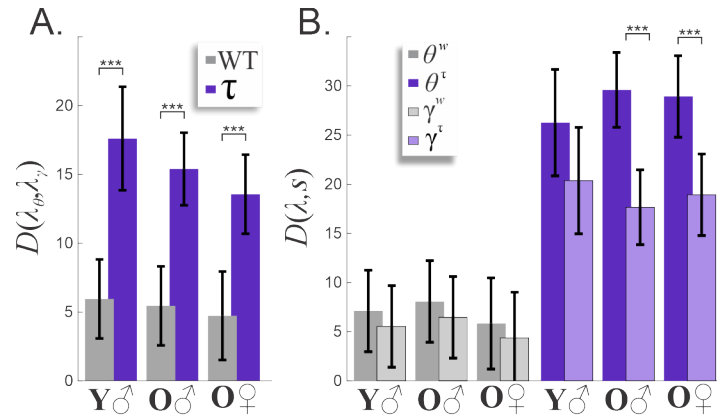


Fig S8. Comparing patterns of θ and γ . **A.** There is a significant increase ($\sim 3\times$) in the LCSS distance between λ_θ and λ_γ in tau-mice, regardless of the mice’s age group or gender. **B.** We compared LCSS distance between λ_θ or λ_γ and the mouse’s speed for each age group (old vs young) and gender (male vs female). The results reveal statistically significant distancing of speed from λ_θ and λ_γ in old tau-mice—for them there exists a behavioral de-coupling from θ - and γ -rhythmicity.

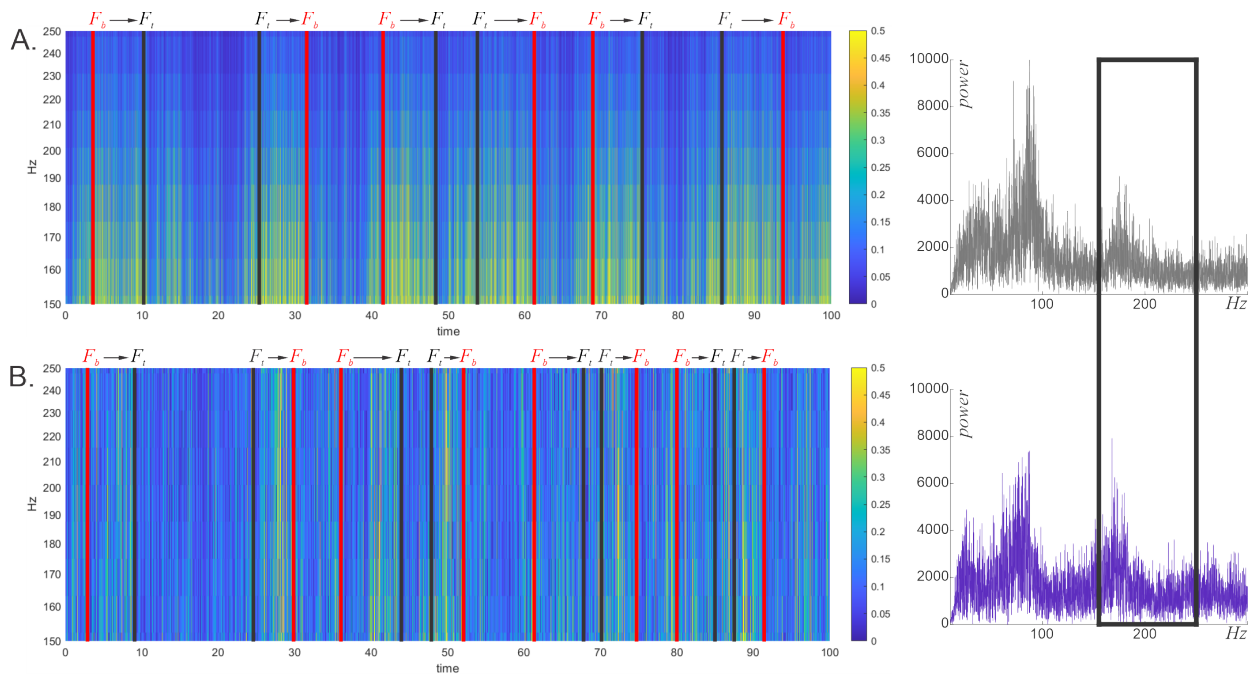


Fig S9. Comparative analysis for high frequency domains. **A.** Continuous wavelet transform comparing high frequency ranges of LFPs recorded from WT (top) and tau (bottom) mice. Vertical red lines marked “ F_b ” and black lines marked “ F_t ” correspond to the bottom and top food wells on Fig. S6. **B.** The fast Fourier transforms for each phenotype and the boxed frequency range capture small differences between WT and tau-rippling, whereas pattern differences are much more explicit (Fig. 10).

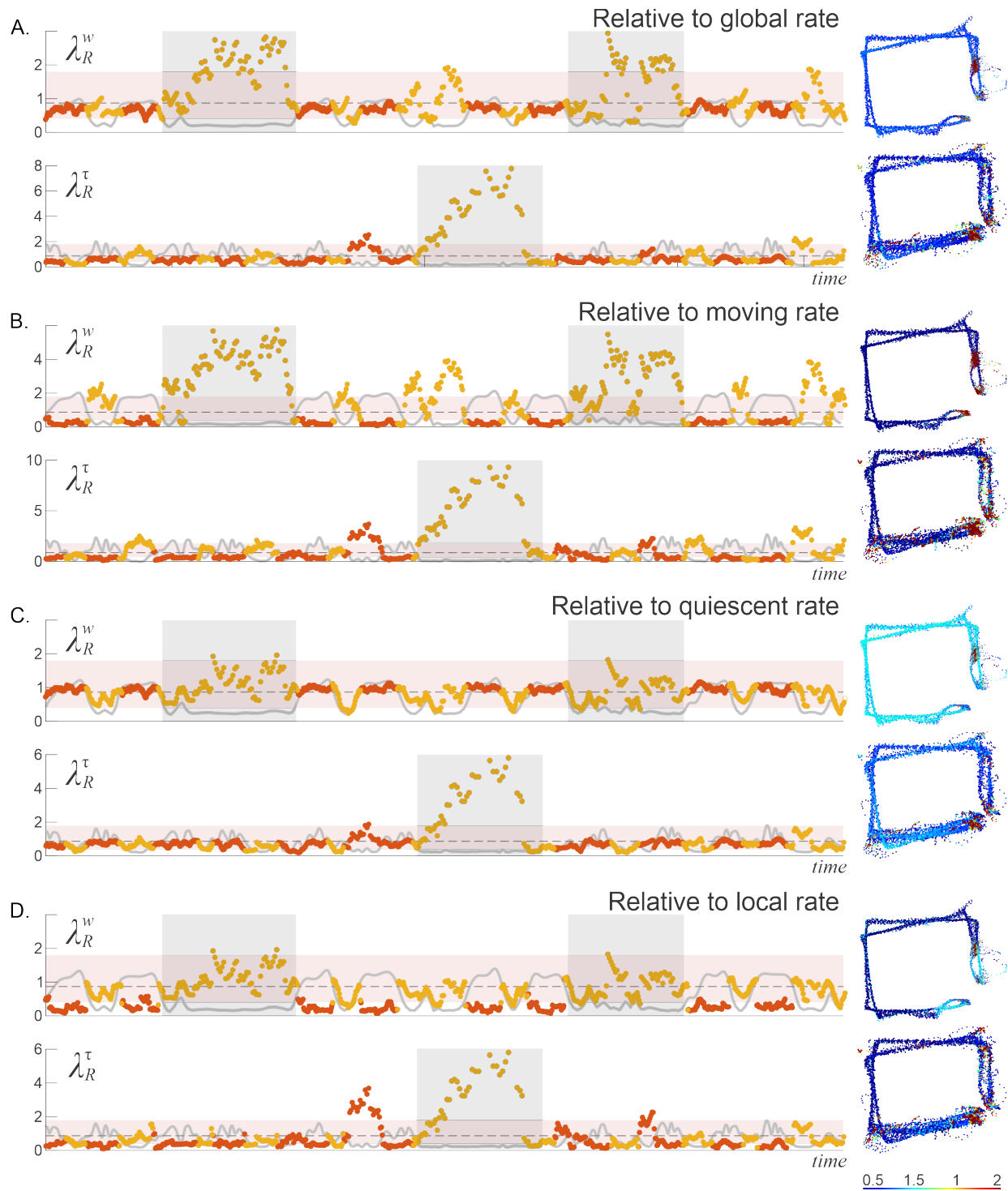


Fig S10. Haphazardness of ripple events referenced to different physiological states in WT and tau-mice.

A. R -patterns calculated for WT (top) and tau (bottom) mice with reference to their respective global rates. WT ripple events are sensitive to changes in movement and quiescence, rising during runs and falling during rest. In contrast, λ_R^τ dissociates from the speed. Spatial maps of λ_R^τ show environmentally specific R -patterning and decreased environmental dependence in tau-mice. **B.** Relative to the activity rate, WT rippling during movement is abnormally adherent to the expected trend, deviating from it during quiescence, while tau-ripples remain as haphazard as they were relative to the global rate, as illustrated by the λ_R^w and λ_R^τ maps on the right. **C.** Relative to quiescence, λ_R^w follows the profile of mouse's speed, whereas λ_R^τ remains unchanged. The spatial maps confirm the sensitivity of R^w -stochasticity to changes in the reference trend. **D.** Haphazardness of R s referenced to the animal's ongoing behavior.

VIII. REFERENCES

- [1] DeTure, M., & Dickson, D. The neuropathological diagnosis of Alzheimer's disease. *Mol Neurodegen.* **14**(1): 32 (2019).
- [2] Perl, D. Neuropathology of Alzheimer's disease. *Mt Sinai J Med.* (77)(1): 32-42 (2010).
- [3] Wenk, G. Neuropathologic changes in Alzheimer's disease. *J Clin Psychiatry.* **64** Suppl 9: 7-10 (2003).
- [4] Targa Dias Anastacio, H., Matosin, N., & Ooi, L. Neuronal hyperexcitability in Alzheimer's disease: what are the drivers behind this aberrant phenotype? *Translational psychiatry*, **12**(1): 257. (2022).
- [5] Bachmann, C., Tetzlaff, T., Duarte, R., & Morrison, A. Firing rate homeostasis counteracts changes in stability of recurrent neural networks caused by synapse loss in Alzheimer's disease. *PLoS Comput. Bio.*, **16**(8): e1007790 (2020).
- [6] Glenner, G., Wong, C. Alzheimer's disease: initial report of the purification and characterization of a novel cerebrovascular amyloid protein. *Biochem Biophys Res Commun.* **120**(3): 885-90 (1984).
- [7] Alzheimer, A., Stelzmann, R., Schnitzlein, H., & Murtagh, F. An English translation of Alzheimer's 1907 paper, *Über eine eigenartige Erkrankung der Hirnrinde.* *Clin Anat.* **8**(6): 429-31 (1995).
- [8] Oddo, S., Caccamo, A., Kitazawa, M., Tseng, B., LaFerla, F. Amyloid deposition precedes tangle formation in a triple transgenic model of Alzheimer's disease. *Neurobiol Aging.* **24**(8): 1063-70 (2003).
- [9] Selkoe, D. Alzheimer's disease: genes, proteins, and therapy. *Physiol Rev.* **81**(2): 741-66 (2001).
- [10] Martinsson, I., Quintino, L., Garcia, M., Konings, S., Torres-Garcia, L., Svanbergsson, A., Stange, O., England, R., Deierborg, T., Li, J., Lundberg, C., Gouras, G. A β /Amyloid Precursor Protein-Induced Hyperexcitability and Dysregulation of Homeostatic Synaptic Plasticity in Neuron Models of Alzheimer's Disease. *Front Aging Neurosci.* **14**: 946297 (2022).
- [11] Frere, S., Slutsky, I. Alzheimer's Disease: From Firing Instability to Homeostasis Network Collapse. *Neuron.* **97**(1): 32-58 (2018).
- [12] Rae-Grant, A., Blume, W., Lau, C., Hachinski, V., Fisman, M., & Merskey, H. The Electroencephalogram in Alzheimer-Type Dementia: A Sequential Study Correlating the Electroencephalogram With Psychometric and Quantitative Pathologic Data. *Archives of Neurology.* **44**(1): 50-4 (1987).
- [13] Liddell, D. Investigations of E.E.G. findings in presenile dementia. *J Neurol Neurosurg Psychiatry.* **21**(3): 173-6 (1958).
- [14] Jelles, B., van Birgelen, J., Slaets, J., Hekster, R., Jonkman, E., & Stam, C. Decrease of non-linear structure in the EEG of Alzheimer patients compared to healthy controls. *Clin Neurophys.* **110**(7): 1159-67 (1999).
- [15] Palop, J., Chin, J., Roberson, E., Wang, J., Thwin, M., Bien-Ly, N., Yoo, J., Ho, K., Yu, G., Kreitzer, A., Finkbeiner, S., Noebels, J., Mucke, L. Aberrant excitatory neuronal activity and compensatory remodeling of inhibitory hippocampal circuits in mouse models of Alzheimer's disease. *Neuron.* **55**(5): 697-711 (2007).
- [16] Born, H., Kim, J., Savjani, R., Das, P., Dabaghian, Y., Guo, Q., Yoo, J., Schuler, D., Cirrito, J., Zheng, H., Golde, T., Noebels, J., Jankowsky, J. Genetic suppression of transgenic APP rescues Hypersynchronous network activity in a mouse model of Alzheimer's disease. *J Neurosci.* **34**(11): 3826-40 (2014).
- [17] Scarmeas, N., Honig, L., Choi, H., Cantero, J., Brandt, J., Blacker, D., Albert, M., Amati, J.,

- Marder, K., Bell, K., Hauser, W., Stern, Y. Seizures in Alzheimer disease: who, when, and how common? *Arch Neurol.* **66**(8): 992-7 (2009).
- [18] Palop, J., Mucke, L. Network abnormalities and interneuron dysfunction in Alzheimer disease. *Nat Rev Neurosci.* **17**(12): 777-792 (2016).
- [19] Pandis, D., Scarmeas, N. Seizures in Alzheimer disease: clinical and epidemiological data. *Epilepsy Curr.* **12**(5): 184-7 (2012).
- [20] Vossel, K., Ranasinghe, K., Beagle, A., Mizuiri, D., Honma, S., Dowling, A., Darwish, S., Van Berlo, V., Barnes, D., Mantle, M., Karydas, A., Coppola, G., Roberson, E., Miller, B., Garcia, P., Kirsch, H., Mucke, L., Nagarajan, S. Incidence and impact of subclinical epileptiform activity in Alzheimer's disease. *Ann Neurol.* **80**(6): 858-870 (2016).
- [21] Hoffman, C., Cheng, J., Ji, D., Dabaghian, Y. Pattern dynamics and stochasticity of the brain rhythms. *Proc. Natl. Acad. Sci.* **120**(14): e2218245120 (2023).
- [22] Ramsden, M., Kotilinek, L., Forster, C., Paulson, J., McGowan, E., SantaCruz, K., Guimaraes, A., Yue, M., Lewis, J., Carlson, G., Hutton, M., & Ashe, K. Age-dependent neurofibrillary tangle formation, neuron loss, and memory impairment in a mouse model of human tauopathy (P301L). *J Neurosci.* **25**(46): 10637-47 (2005).
- [23] SantaCruz, K., Lewis, J., Spires, T., Paulson, J., Kotilinek, L., Ingelsson, M., Guimaraes, A., DeTure, M., Ramsden, M., McGowan, E., Forster, C., Yue, M., Orne, J., Janus, C., Mariash, A., Kuskowski, M., Hyman, B., Hutton, M., & Ashe, K. Tau Suppression in a Neurodegenerative Mouse Model Improves Memory Function. *Science.* **309**(5733): 476-81 (2005).
- [24] Cheng, J. & Ji, D. Rigid firing sequences undermine spatial memory codes in a neurodegenerative mouse model. *eLife*, **2**: e00647 (2013).
- [25] Ciupek, S., Cheng, J., Ali, Y., Lu, H., & Ji, D. Progressive functional impairments of hippocampal neurons in a tauopathy mouse model. *J. Neurosci.* **35**(21): 8118–8131 (2015).
- [26] Kolmogorov, A. Sulla determinazione empirica di una legge di distribuzione. *Giornale dell'Istituto Italiano degli Attuari*, **4**(1): 83-91 (1933).
- [27] Arnold, V. Orbits' statistics in chaotic dynamical systems. *Nonlinearity* **21**: T109 (2008).
- [28] Arnold, V. Empirical study of stochasticity for deterministic chaotic dynamics of geometric progressions of residues. *Funct. Anal. Other Math.* **2**: 139-149 (2009).
- [29] Arnold, V. To what extent are arithmetic progressions of fractional parts stochastic? *Russian Mathematical Surveys* **63**: 205 (2008).
- [30] Rickert, J., Oliveira, S., Vaadia, E., Aertsen, A., Rotter, S., Mehring, C. Encoding of movement direction in different frequency ranges of motor cortical local field potentials. *J Neurosci.* **25**(39): 8815-24 (2005).
- [31] Baker, S., Kilner, J., Pinches, E., Lemon, R. The role of synchrony and oscillations in the motor output. *Exp Brain Res.* **128**(1-2): 109-17 (1999).
- [32] Murthy, V., Fetz, E. Oscillatory activity in sensorimotor cortex of awake monkeys: synchronization of local field potentials and relation to behavior. *J Neurophysiol.* **76**(6): 3949-67 (1996).
- [33] Buzsáki, G. Theta oscillations in the hippocampus. *Neuron* **33**: 325-340 (2002).
- [34] Burgess, N. & O'Keefe, J. The theta rhythm. *Hippocampus* **15**(7): 825-826 (2005).
- [35] Buzsáki, G. Theta rhythm of navigation: link between path integration and landmark navigation, episodic and semantic memory. *Hippocampus.* **15**(7): 827-40 (2005).
- [36] Buzsáki, G., Moser, E. Memory, navigation and theta rhythm in the hippocampal-entorhinal system. *Nat. Neurosci.* **16**(2): 130-8 (2013).
- [37] Cacucci, F., Lever, C., Wills, T., Burgess, N., O'Keefe, J. Theta-modulated place-by-direction cells in the hippocampal formation in the rat. *J. Neurosci.*, **24**(38): 8265-77 (2004).

- [38] Itskov, V., Pastalkova, E., Mizuseki, K., Buzsáki, G., Harris, K. Theta-mediated dynamics of spatial information in hippocampus. *J. Neurosci.*, **28**(23): 5959-64 (2008).
- [39] Osbert, C., Berj, L. Theta phase precession and phase selectivity: a cognitive device description of neural coding. *J Neural Eng.* **6**(3): 036002 (2009).
- [40] Jelic, V., Johansson, S., Almkvist, O., Shigeta, M., Julin, P., Nordberg, A., Winblad, B., Wahlund, L. Quantitative electroencephalography in mild cognitive impairment: longitudinal changes and possible prediction of Alzheimer's disease. *Neurobiology of Aging.* **21**(4): 533-40 (2000).
- [41] Bennys, K., Rondouin, G., Vergnes, C., Touchon, J. Diagnostic value of quantitative EEG in Alzheimer's disease. *Neurophysiol Clin.* **31**(3): 153-60 (2001).
- [42] Colgin, L. Mechanisms and functions of theta rhythms. *Ann. Rev. Neurosci.*, **36**:295–312 (2013).
- [43] Joshi, A., Denovellis, E., Mankili, A., Meneksedag, Y., Davidson, T., Gillespie, A., Guidera, J., Roumis, D., Frank, L. Dynamic synchronization between hippocampal representations and stepping. *Nature.* **617**(7959): 125-131 (2023).
- [44] Bender, F., Gorbati, M., Cadavieco, M., Denisova, N., Gao, X., Holman, C., Korotkova, T., Ponomarenko, A. Theta oscillations regulate the speed of locomotion via a hippocampus to lateral septum pathway. *Nat Commun.* **6**: 8521 (2015).
- [45] Fuhrmann, F., Justus, D., Sosulina, L., Kaneko, H., Beutel, T., Friedrichs, D., Schoch, S., Schwarz, M., Fuhrmann, M., Remy, S. Locomotion, Theta Oscillations, and the Speed-Related Firing of Hippocampal Neurons Are Controlled by a Medial Septal Glutamatergic Circuit. *Neuron.* **86**(5): 1253-64 (2015).
- [46] Vlachos, M., Kollios, G., & Gunopulos, D. Discovering similar multidimensional trajectories. *Proceedings 18th International Conference on Data Engineering.* 673-684 (2002).
- [47] Khan, R., Ahmad, M., & Zakarya, M. Longest Common Subsequence Based Algorithm for Measuring Similarity Between Time Series: A New Approach. *World Applied Sciences Journal.* **24** (2013).
- [48] Morse, M., Patel, J. An efficient and accurate method for evaluating time series similarity. *ACM SIGMOD Conference.* (2007).
- [49] O'Keefe, J., Dostrovsky, J. The hippocampus as a spatial map. Preliminary evidence from unit activity in the freely-moving rat. *Brain Research.* **34**(1): 171–75 (1971).
- [50] Moser, E. Kropff, E. & Moser, M.-B. Place Cells, Grid Cells, and the Brain's Spatial Representation System. *Annu Rev Neurosci.* **31**(1): 69-89 (2008).
- [51] Fenton, A., Kao, H., Neymotin, S., Olypher, A., Vayntrub, Y., Lytton, W., Ludvig, N. Unmasking the CA1 ensemble place code by exposures to small and large environments: more place cells and multiple, irregularly arranged, and expanded place fields in the larger space. *J Neurosci.* **28**(44): 11250-62 (2008).
- [52] Redish, A., Battaglia, F., Chawla, M., Ekstrom, A., Gerrard, J., Lipa, P., Rosenzweig, E., Worley, P., Guzowski, J., McNaughton, B., Barnes, C. Independence of firing correlates of anatomically proximate hippocampal pyramidal cells. *J Neurosci.* **21**(5): RC134 (2001).
- [53] Amaral, D. Emerging principles of intrinsic hippocampal organization. *Curr Opin Neurobiol.* **3**(2): 225-9 (1993).
- [54] McNaughton, B., Barnes, C., Meltzer, J., Sutherland, R. Hippocampal granule cells are necessary for normal spatial learning but not for spatially-selective pyramidal cell discharge. *Exp Brain Res.* **76**(3): 485-96 (1989).
- [55] Geisler, C., Diba, K., Pastalkova, E., Mizuseki, K., Royer, S., Buzsáki, G. Temporal delays among place cells determine the frequency of population theta oscillations in the hippocampus. *Proc. Natl. Acad. Sci.* **107**(17): 7957-62 (2010).
- [56] Dragoi, G., Buzsáki, G. Temporal encoding of place sequences by hippocampal cell assemblies.

- Neuron*. **50**(1): 145-57 (2006).
- [57] Jensen, O., Lisman, J. Position reconstruction from an ensemble of hippocampal place cells: contribution of theta phase coding. *J Neurophysiol*. **83**(5): 2602-9 (2000).
- [58] Brown, E., Frank, L., Tang, D., Quirk, M., Wilson, M. A statistical paradigm for neural spike train decoding applied to position prediction from ensemble firing patterns of rat hippocampal place cells. *J Neurosci*. **18**(18): 7411-25 (1998).
- [59] Foster, D., & Wilson, M. Reverse replay of behavioural sequences in hippocampal place cells during the awake state *Nature* **440**: 680–683 (2006).
- [60] Karlsson, M. & Frank L. Awake replay of remote experiences in the hippocampus. *Nat. Neurosci*. **12**: 913-918 (2009).
- [61] Carr, M., Jadhav, S. & Frank, L. Hippocampal replay in the awake state: a potential substrate for memory consolidation and retrieval, *Nat. Neurosci.*, **14**: 147-153 (2011).
- [62] Singer, A., Carr, M. Karlsson, M. & Frank, L. Hippocampal SWR Activity Predicts Correct Decisions during the Initial Learning of an Alternation Task. *Neuron* **77**: 1163-1173 (2013).
- [63] Denovellis, E., Gillespie, A., Coulter, M., Sosa, M., Chung, J., Eden, U. & Frank, L. Hippocampal replay of experience at real-world speeds. *Elife* **10**:e64505 (2021).
- [64] Nádasdy, Z., Hirase, H., Czurkó, A., Csicsvari, J., Buzsáki, G. Replay and time compression of recurring spike sequences in the hippocampus. *J Neurosci*. **19**(21): 9497-507 (1999).
- [65] Lee, A., Wilson, M. Memory of sequential experience in the hippocampus during slow wave sleep. *Neuron*. **36**(6): 1183-94 (2002).
- [66] Ji, D. & Wilson, M. Coordinated memory replay in the visual cortex and hippocampus during sleep, *Nat. Neurosci*, **10**(1): 100–107 (2007).
- [67] Diba, K., Buzsáki, G. Forward and reverse hippocampal place-cell sequences during ripples. *Nat Neurosci*. **10**(10): 1241-2 (2007).
- [68] Davidson, T., Kloosterman, F., Wilson, M. Hippocampal replay of extended experience. *Neuron*. **63**(4): 497-507 (2009).
- [69] Gupta, A., van der Meer, M., Touretzky, D. & Redish, A. Hippocampal replay is not a simple function of experience. *Neuron*, **65**(5): 695–705 (2010).
- [70] Buhry, L., Azizi, A., & Cheng, S. Reactivation, replay, and preplay: how it might all fit together. *Neural plasticity*, 203462 (2011).
- [71] Stella, F., Baracskay, P., O'Neill, J. & Csicsvari, J. Hippocampal Reactivation of Random Trajectories Resembling Brownian Diffusion. *Neuron*, **102**(2): 450–461.e7 (2019).
- [72] Kudrimoti, H., Barnes, C., & McNaughton B. Reactivation of hippocampal cell assemblies: effects of behavioral state, experience, and EEG dynamics. *J Neurosci*. **19**: 4090–101 (1999).
- [73] O'Neil, J., Senior, A., Allen, K., Huxter, J. & Csicsvari, J. Reactivation of experience-dependent cell assembly patterns in the hippocampus. *Nat. Neurosci*. **11**: 209–216 (2008).
- [74] Ólafsdóttir, H., Bush, D. & Barry, C. The Role of Hippocampal Replay in Memory and Planning. *Current Biology*, **28**(1): R37-R50 (2018).
- [75] E. Pastalkova, V. Itskov, A. Amarasingham and G. Buzsaki. Internally Generated Cell Assembly Sequences in the Rat Hippocampus. *Science* **321**: 1322 (2008).
- [76] Taxidis, J., Anastassiou Costas, A., Diba, K. & Koch, C. Local Field Potentials Encode Place Cell Ensemble Activation during Hippocampal Sharp Wave Ripples. *Neuron*, **87**(3): 590-604 (2015).
- [77] Ylinen, A., Bragin, A., Nádasdy, Z., Jandó, G., Szabó, I., Sik, A., Buzsáki, G. Sharp wave-associated high-frequency oscillation (200 Hz) in the intact hippocampus: network and intracellular mechanisms. *J Neurosci*. **15**(1 Pt 1): 30-46 (1995).
- [78] Csicsvari, J., Hirase, H., Czurkó, A., Mamiya, A., Buzsáki, G. Oscillatory coupling of hippocampal

- pyramidal cells and interneurons in the behaving Rat. *J Neurosci.* **19**(1): 274-87 (1999).
- [79] Klausberger, T., Somogyi, P. Neuronal diversity and temporal dynamics: the unity of hippocampal circuit operations. *Science.* **321**(5885): 53-7 (2008).
- [80] Squire, L. Memory and the hippocampus: a synthesis from findings with rats, monkeys, and humans. *Psychol Rev.* **99**(2): 195-231 (1992).
- [81] Remondes, M., Schuman, E. Role for a cortical input to hippocampal area CA1 in the consolidation of a long-term memory. *Nature.* **431**(7009): 699-703 (2004).
- [82] Manns, J., Zilli, E., Ong, K., Hasselmo, M, Eichenbaum, H. Hippocampal CA1 spiking during encoding and retrieval: relation to theta phase. *Neurobiol Learn Mem.* **87**(1): 9-20 (2007).
- [83] Moser, E., Kropff, E., Moser, M. Place cells, grid cells, and the brain's spatial representation system. *Ann. Rev. Neurosci.* **31**: 69-89 (2008).
- [84] Klausberger, T., Magill, P., Márton, L., Roberts, J., Cobden, P., Buzsáki, G., Somogyi, P. Brain-state- and cell-type-specific firing of hippocampal interneurons in vivo. *Nature.* **421**(6925): 844-8 (2003).
- [85] Jinno, S., Klausberger, T., Marton, L., Dalezios, Y., Roberts, J., Fuentealba, P., Bushong, E., Henze, D., Buzsáki, G., Somogyi, P. Neuronal diversity in GABAergic long-range projections from the hippocampus *J Neurosci.* **27**: 8790–8804 (2007).
- [86] Varga, C., Golshani, P., Soltesz, I. Frequency-invariant temporal ordering of interneuronal discharges during hippocampal oscillations in awake mice. *Proc. Natl. Acad. Sci.* **109**(40): E2726-34 (2012).
- [87] Colgin, L., Denninger, T., Fyhn, M., Hafting, T., Bonnevie, T., Jensen, O., Moser, M-B. & Moser, E. Frequency of gamma oscillations routes flow of information in the hippocampus. *Nature* **462**: 353-357 (2009).
- [88] Jia, X., Kohn, A. Gamma rhythms in the brain. *PLoS Biol.* **9**(4): e1001045 (2011).
- [89] Nikoli, D., Fries, P. & Singer, W. Gamma oscillations: precise temporal coordination without a metronome. *Trends Cogn Sci.* **17**: 54-55 (2013).
- [90] Bieri, K., Bobbitt, K., Colgin, L. Slow and Fast Gamma Rhythms Coordinate Different Spatial Coding Modes in Hippocampal Place Cells. *Neuron.* **82**(3): 670-81 (2014).
- [91] Colgin, L. & Moser E. Gamma oscillations in the hippocampus. *Physiology* **25**: 319-329 (2010).
- [92] Goutagny, R., Gu, N., Cavanagh, C., Jackson, J., Chabot, J., Quirion, R., Krantic, S., Williams, S. Alterations in hippocampal network oscillations and theta-gamma coupling arise before A β overproduction in a mouse model of Alzheimer's disease. *European J Neurosci.* **37**(12): 1896-902 (2013).
- [93] Iaccarino, H., Singer, A., Martorell, A., Rudenko, A., Gao, F., Gillingham, T., Mathys, H., Seo, J., Kritskiy, O., Abdurrob, F., Adaikkan, C., Canter, R., Rueda, R., Brown, E., Boyden, E., Tsai, L. Gamma frequency entrainment attenuates amyloid load and modifies microglia. *Nature.* **540**(7632): 230-235 (2016).
- [94] Mably, A., Gereke, B., Jones, D., Colgin, L. Impairments in spatial representations and rhythmic coordination of place cells in the 3xTg mouse model of Alzheimer's disease. *Hippocampus.* **27**(4): 378-392 (2017).
- [95] Canolty, R., Edwards, E., Dalal, S., Soltani, M., Nagarajan, S., Kirsch, H., Berger, M., Barbaro, N., Knight, R. High Gamma Power Is Phase-Locked to Theta Oscillations in Human Neocortex. *Science.* **313**(5793): 1626-8 (2006).
- [96] Pastoll, H., Solanka, L., van Rossum, M., Nolan, M. Feedback inhibition enables θ -nested γ oscillations and grid firing fields. *Neuron.* **77**(1): 141-54 (2013).
- [97] Sirota, A., Montgomery, S., Fujisawa, S., Isomura, Y., Zugaro, M, Buzsáki, G. Entrainment of neocortical neurons and gamma oscillations by the hippocampal theta rhythm. *Neuron.* **60**(4): 683-97 (2008).
- [98] Canolty, R., Knight, R. The functional role of cross-frequency coupling. *Trends Cog. Sci.* **14**(11):

- 506-15(2010).
- [99] Benchenane, K., Peyrache, A., Khamassi, M., Tierney, P., Gioanni, Y., Battaglia, F. & Wiener, S. Coherent Theta Oscillations and Reorganization of Spike Timing in the Hippocampal- Prefrontal Network upon Learning. *Neuron* **66**: 921-936 (2010).
 - [100] Zhang, X., Zhong, W., Brankack, J., Weyer, S., Müller, U., Tort, A., Draguhn, A. Impaired theta-gamma coupling in APP-deficient mice. *Scientific reports*. **6**: 21948 (2016).
 - [101] Goodman, M., Kumar, S., Zomorodi, R., Ghazala, Z., Cheam, A., Barr, M., Daskalakis, Z., Blumberger, D., Fischer, C., Flint, A., Mah, L., Herrmann, N., Bowie, C., Mulsant, B., Rajji, T. Theta-Gamma Coupling and Working Memory in Alzheimer's Dementia and Mild Cognitive Impairment. *Front Aging Neurosci*. **10**: 101 (2018).
 - [102] Buzsáki, G. Hippocampal sharp wave-ripple: A cognitive biomarker for episodic memory and planning. *Hippocampus*. **25**(10): 1073-188 (2015).
 - [103] Csicsvari, J., Dupret, D. Sharp wave/ripple network oscillations and learning-associated hippocampal maps. *Philos. Trans. R. Soc. B*. **369**(1635): (2014).
 - [104] Joo, H., Frank, L. The hippocampal sharp wave-ripple in memory retrieval for immediate use and consolidation. *Nat. Rev. Neurosci*. **19**(12): 744-57 (2018).
 - [105] Leonard, T., Mikkila, J., Eskandar, E., Gerrard, J., Kaping, D., Patel, S., Womelsdorf, T., Hoffman, K. Sharp Wave Ripples during Visual Exploration in the Primate Hippocampus. *J Neurosci*. **35**(44): 14771-82 (2015).
 - [106] Fernández-Ruiz, A., Oliva, A., Fermino de Oliveira, E., Rocha-Almeida, F., Tingley, D., Buzsáki, G. Long-duration hippocampal sharp wave ripples improve memory. *Science*. **364**(6445): 1082-1086 (2019).
 - [107] Girardeau, G., Benchenane, K., Wiener, S., Buzsáki, G. & Zugaro, M. Selective suppression of hippocampal ripples impairs spatial memory. *Nat. Neurosci*. **12**, 1222-1223 (2010).
 - [108] Schreiter-Gasser, U., Gasser, T., Ziegler, P. Quantitative EEG analysis in early onset Alzheimer's disease: correlations with severity, clinical characteristics, visual EEG and CCT. *Clin. Neurophysiol*. **90**(4): 267-272 (1994).
 - [109] Girardeau, G., Zugaro, M. Hippocampal ripples and memory consolidation. *Curr. Opin. Neurobiol* **21**, 452-459 (2001).
 - [110] Roux, L., Hu, B., Eichler, R., Stark, E. & Buzsáki, G. Sharp wave ripples during learning stabilize the hippocampal spatial map. *Nat. Neurosci*. **20**:845-853 (2017).
 - [111] Sadowski, J., Jones, M. & Mellor, J. Sharp-Wave Ripples Orchestrate the Induction of Synaptic Plasticity during Reactivation of Place Cell Firing Patterns in the Hippocampus. *Cell reports* **14**, 1916-1929 (2016).
 - [112] Caccavano, A., Bozzelli, P. L., Forcelli, P. A., Pak, D. T. S., Wu, J. Y., Conant, K., Vicini, S. Inhibitory Parvalbumin Basket Cell Activity is Selectively Reduced during Hippocampal Sharp Wave Ripples in a Mouse Model of Familial Alzheimer's Disease. *J Neurosci*. **40**(26): 5116–5136 (2020).
 - [113] Witton, J., Staniaszek, L., Bartsch, U., Randall, A., Jones, M., Brown, J. Disrupted hippocampal sharp-wave ripple-associated spike dynamics in a transgenic mouse model of dementia. *J Physiol*. **594**(16): 4615-30 (2016).
 - [114] Arenas, A., Dáz-Guilera, A., Kurths, J., Moreno, Y. & Zhou, C., Synchronization in complex networks. *Physics Reports* **469**: 93-153 (2008).
 - [115] Liao, X. et al. Pattern formation in oscillatory complex networks consisting of excitable nodes. *Physical Review E* **83**: 056204 (2011).
 - [116] Mi, Y. et al. Long-period rhythmic synchronous firing in a scale-free network. *Proc. Natl. Acad. Sci*. **110**: E4931-E4936 (2013).

- [117] Restrepo, J., Ott, E. & Hunt, B. Onset of synchronization in large networks of coupled oscillators. *Physical Review E* **71**: 036151 (2005).
- [118] Burton, S., Ermentrout, G. & Urban, N. Intrinsic heterogeneity in oscillatory dynamics limits correlation-induced neural synchronization. *J Neurophysiol* **108** (2012).
- [119] Bezaire, M., Raikov, I., Burk, K., Vyas, D. & Soltesz, I. Interneuronal mechanisms of hippocampal theta oscillations in a full-scale model of the rodent CA1 circuit. *eLife*, **5**: e18566 (2016).
- [120] Buzsáki, G. & Wang, X. Mechanisms of gamma oscillations. *Ann. Rev. Neurosci* **35**: 203-225 (2012).
- [121] Jun, H., Bramian, A., Soma, S., Saito, T., Saido, T., Igarashi, K. Disrupted Place Cell Remapping and Impaired Grid Cells in a Knock-in Model of Alzheimer’s Disease. *Neuron*. **107**(6): 1095-1112.e6 (2020).
- [122] Cacucci, F., Yi, M., Wills, T., Chapman, P., O’Keefe, J. Place cell firing correlates with memory deficits and amyloid plaque burden in Tg2576 Alzheimer mouse model. *Proc. Natl. Acad. Sci.* **105**(22): 7863-8 (2008).
- [123] Arnold, V. Topology and statistics of arithmetic and algebraic formulae. *Russian Math. Surv.* **58**(4) 637–664 (2003).
- [124] Arnold, V. *Lectures and Problems: A Gift to Young Mathematicians*, American Math Society, Providence (2015).
- [125] Stephens, M. Introduction to Kolmogorov (1933) On the Empirical Determination of a Distribution. In: Kotz S., Johnson N.L. (eds) *Breakthroughs in Statistics*. Springer Series in Statistics. Springer, New York, NY (1992).
- [126] Vrbik, J. Small-sample corrections to Kolmogorov–Smirnov test statistic. *Pioneer Journal of Theoretical and Applied Statistics*, **15**(1–2): 15–23 (2018).
- [127] Bol’shev, L. Asymptotically Pearson Transformations *Theory Probab. Appl.*, **8**(2): 121-146 (1963).